Design and simulation of the rotating test rig in the INDUFLAP project

Barlas, Athanasios; Aagaard Madsen , Helge; Løgstrup Andersen, Tom

Publication date:
2014

Document Version
Publisher's PDF, also known as Version of record

Design and simulation of the rotating test rig in the INDUFLAP project

Department of Wind Energy
E Report 2015

Thanasis K. Barlas, Helge A. Madsen, Tom L. Andersen

DTU Vindenergi-E-0063(EN)

December2014

DTU Vindenergi
Institut for Vindenergi

Authors: Thanasis K. Barlas, Helge A. Madsen
Title: Design and simulation of the rotating test rig in the INDUFLAP project
Department: Institut for Vindenergy

Summary (max 2000 characters):
The general description and objectives of the rotating test rig at the Risø campus of DTU are presented, as used for the aeroelastic testing of a controllable rubber trailing edge flap (CRTEF) system in the INDUFLAP project. The design of all new components is presented, including the electrical drive, the pitch system, the boom, and the wing/flap section. The overall instrumentation of the components used for the aeroelastic testing is described. Moreover, the aeroelastic model simulating the setup is described, and predictions of steady and dynamic loading along with the aeroelastic analysis of the setup are documented. Finally, the measured structural dynamics of the rig setup are presented.

DTU Vindenergi-E-0063(EN)
2014

Contract no.:

Project no.:
43031

Sponsorship:
EUDP

Front page:
Photo of the rotating rig

Pages: 89
Tables: 11
References: 5

Danmarks Tekniske Universitet
DTU Vindenergi
Nils Koppels Allé
Bygning 403
2800 Kgs. Lyngby
Phone

www.vindenergi.dtu.dk

Preface

This report is a collection of all design and modelling work related to the rotating test rig at the Risø campus of DTU as used for the purpose of the aeroelastic testing of a flap control system in the INDUFLAP project.

Roskilde, December 2014

Thanasis K. Barlas
Researcher

Content

Summary

This report serves as a summary documenting the design of the rotating test rig components, the instrumentation for testing, the aeroelastic modelling and simulations of the setup and experimental data on its structural dynamics.

1. Introduction, background and objectives

In this section, the rotating test rig is introduced, together with background information and general objectives in the context of the INDUFLAP project.

Introduction

The idea of a rotating test rig for aerodynamic, aeroelastic, aeroservoelastic and aeroacoustic experiments had been proposed in the AED group of DTU Wind Energy, where a description of such a facility has been presented in 2009. However, in preparation of the EUDP 2011 project INDUFLAP it was found that an outdoor rotating test rig for testing and of characterizing trailing edge flaps was desirable. Although it was originally planned to have the test rig ready for operation in the spring 2012, the final setup was installed and operational in the summer of 2014.

Background information

In order to fill in the gap between full-scale MW experiments and wind tunnel tests the 100 KW Tellus turbine (**Figure 1**) situated at the test field at Risø campus plays an important role as a test bed for aerodynamic and aeroservoelastic experiments.

The rotor on the turbine is replaced by an elastic beam. On the outer part of the beam different elements to be tested can be mounted for characterization of aerofoil characteristics based on pressure measurements and testing of pitch and flap control systems.

Besides the main beam, a counter weight is mounted to balance the beam and the aerofoil section. During the measurements the turbine is motored and a frequency converter is added in order to control the rotational speed.

Main advantages of the setup include:

- easy access to the test rig for Risø DTU and DTU researchers and for students
- a size where installation of equipment does not require a huge crane
- very suitable to perform aeroelastic experiments
- very suitable to test prototypes of inflow sensors, flaps, aerodynamic devices
- with a lift installed on the turbine, easy access to inspect the equipment on the blade section
- the measurement of aerodynamic characteristics in free wind could be an important supplement to wind tunnel measurements on aerofoil sections

Figure 1 - The 100kW Tellus turbine at the Risø campus test field.

Objectives

The overall design of the rotating rig setup for the INDUFLAP project purposes comprises a 2.2m span-wise length and 1m chord-wise length NACA0015 aerofoil section, with a 0.15m chord-wise length Controllable Rubber Trailing Edge Flap (CRTEF) mounted at the end of an 8m long beam, which is fitted at a modified setup of the old Tellus 100kW turbine (**Figure 2**). The main objective is to conduct tests of the controllable rubber trailing edge flap (CRTEF) system under realistic inflow conditions in the rotating test rig.

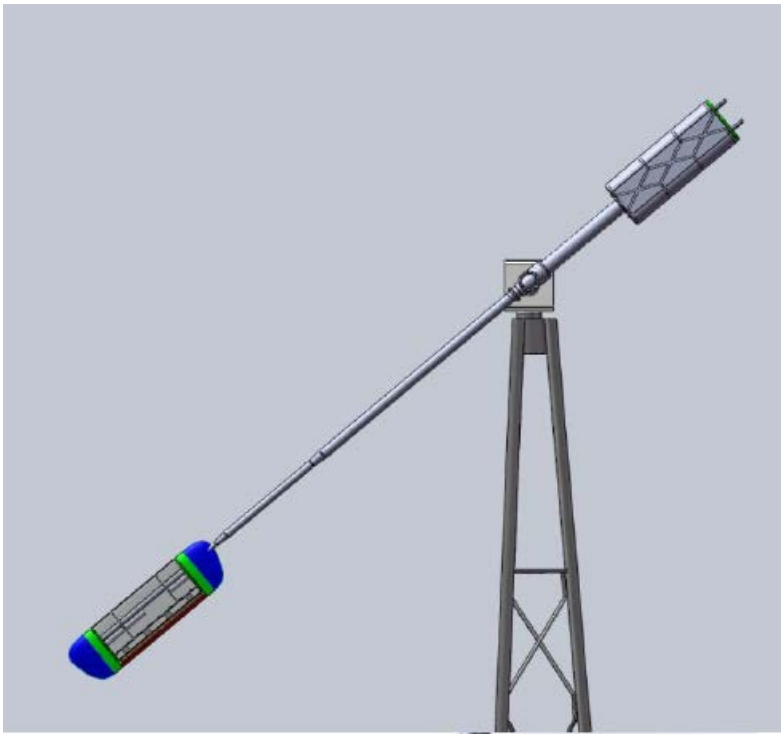

Figure 2 - Concept sketch of the rotating rig setup for the INDUFLAP project.

The objectives from the WP4 of the INDUFLAP project related to the setup include the:

- overall design of test rig based on aeroelastic simulations
- detailed design of boom including pitch system and attachment of blade section
- manufacturing of and installation of boom and power system on the 100 kW Tellus turbine
- instrumentation of test rig and blade/flap sections
- testing of different flaps, control systems and sensor systems

This report includes a summary of all background information on the design of the components of the test rig, together with the aeroelastic model setup for simulating it and the experimental data on the dynamics of the structure.

2. Design of the boom

In this section, the design of the boom for the rotating test rig is presented.

Boom assembly geometry

The boom is part of the assembly of the new designed and manufactured components for the rig, together with the wing section, the hub and the counterweight (**Figure 3**). The boom, the counter-weight and hub assemblies are described in this section. The pitch system design is described in detail in **Section 2**, whereas the wing test section which is attached at the outer boom section is described in detail in **Section 5**.

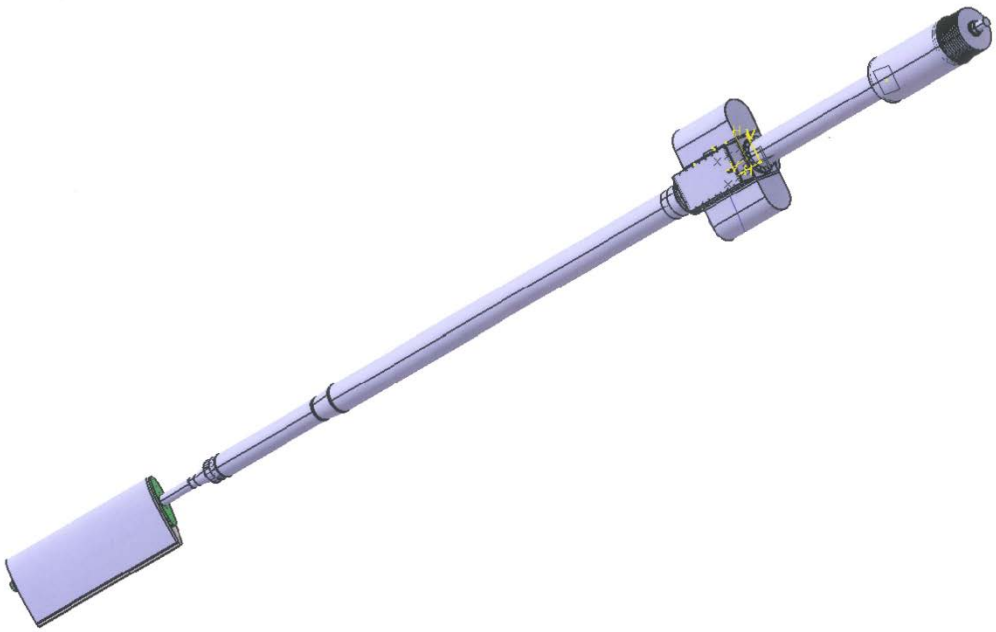

Figure 3 - The 3D drawing of the rotor assembly including the boom, wing section, hub and counterweight.

Component design - boom

The boom consists of four thin-walled tubular sections (three of aluminium alloy 6082 and one of steel St52) and the connection pieces and flanges between them. The technical drawing of the boom assembly is shown in **Figure 4**.

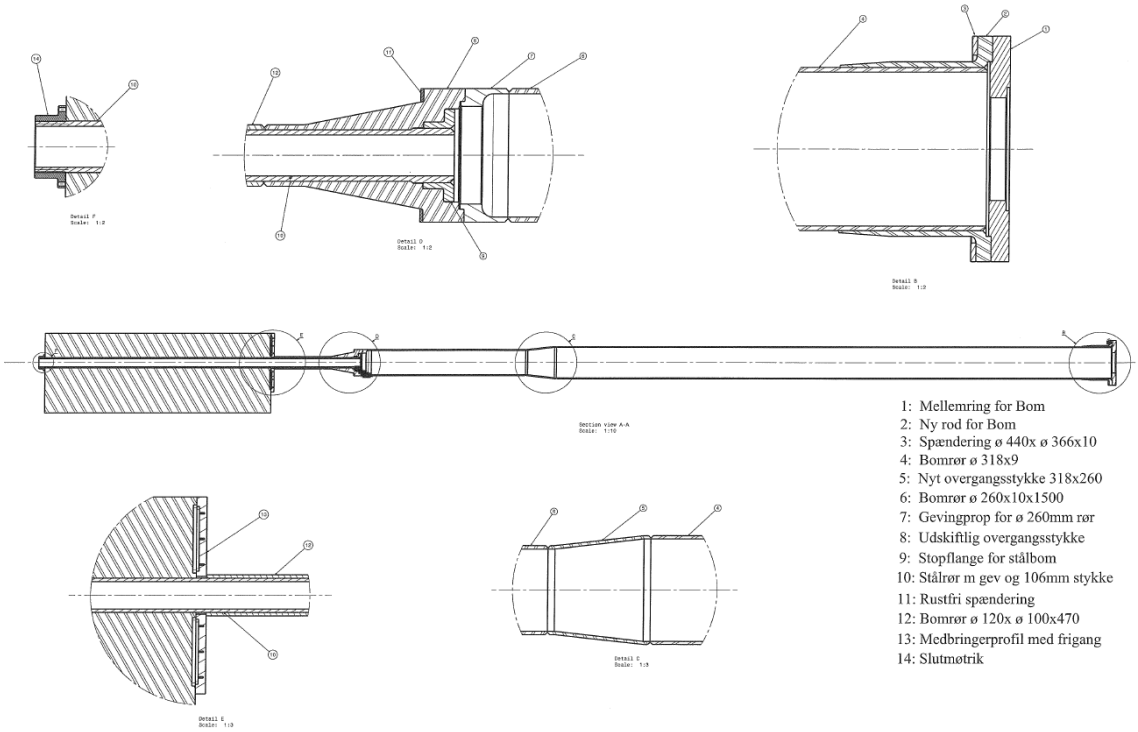

Figure 4 - Technical drawing of the boom assembly.

The list of the tubular section components comprising the boom assembly is presented in **Table 1**, together with their characteristic parameters.

Table 1 Boom component parameters.

Part	Length [m]	Inner diameter [m]	Outer diameter [m]	Mass [kg]
Boom section 1	5.439	0.300	0.320	47.47
Boom section 2	1.500	0.240	0.260	31.82
Boom section 3	0.500	0.120	0.100	4.52
Boom section 4	3.130	0.100	0.080	70.10

The boom has been initially dimensioned according to calculated stress assuming thin walled circular section profiles at the different span-wise locations and utilizing the predicted sectional normal force and bending moment distributions from an early HAWC2 aeroelastic model. IEC Class IIIA site conditions are have been used, where extreme loads come from Normal Turbulent Series (NTM), with a focus on 1, 5 and 50 year extreme values. Safety factors of 1.25 for loads in DLC 1.1 and of 1.1 for materials are used. The calculated max stress levels have been compared to the 0,2% proof strength of the material (Al 60829 and St 52). The predicted

dynamic stress along the span for aluminium and steel designs is compared to the material strength in **Figure 5**.

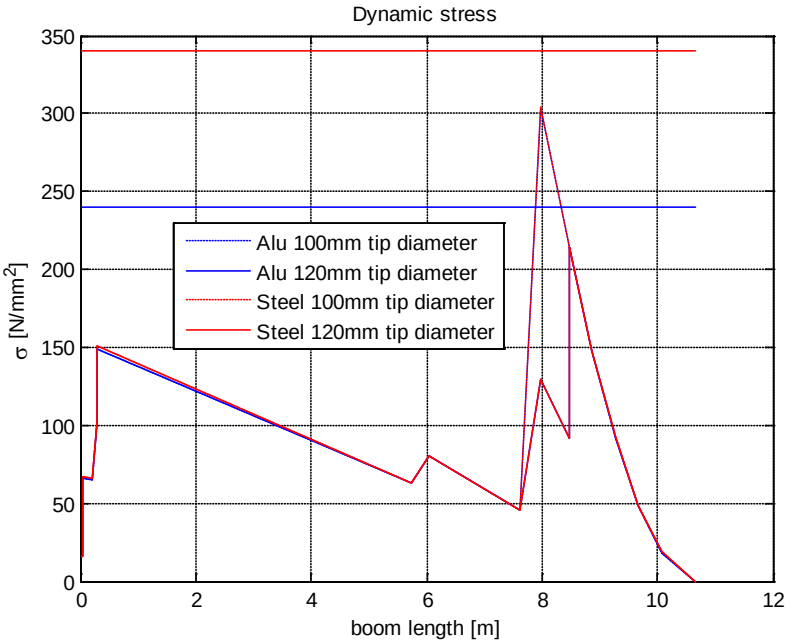

Figure 5 – Computed maximum dynamic stress along the boom and comparison to material strength levels.

Component design – counter-weight

The counter-weight consists of two thin-walled tubular sections together with an assembly of a rod with weight discs (steel St52) and the connection pieces and flanges between them. The technical drawings of the counter-weight assembly are shown in **Figure 6**, **Figure 7**, **and Figure 8**.

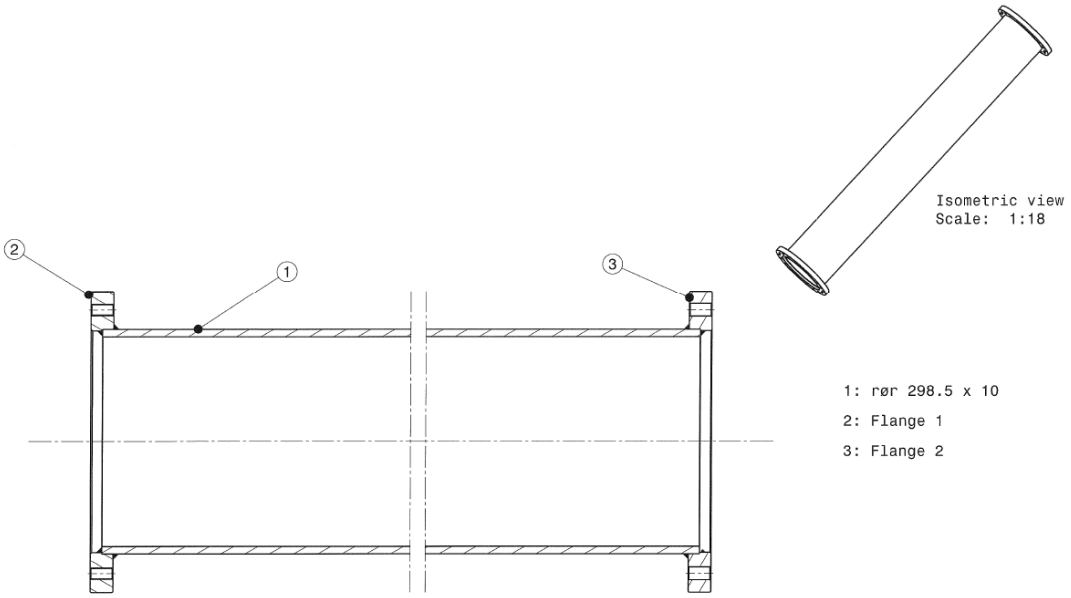

Figure 6 – Technical drawing of the first counter-weight section.

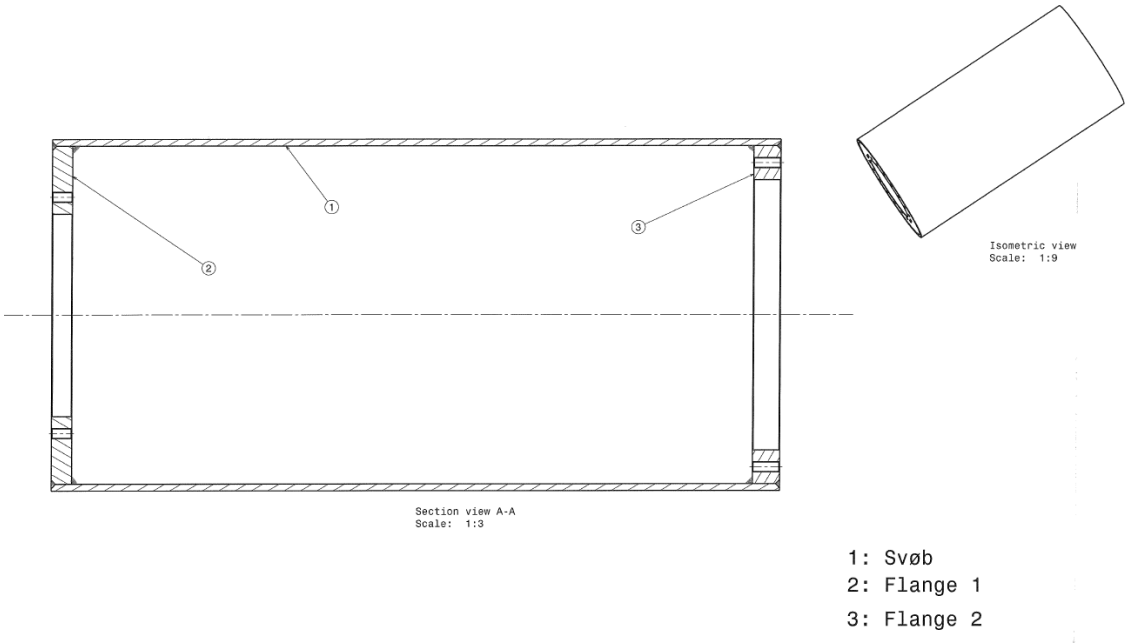

Figure 7 – Technical drawing of the second counter-weight section.

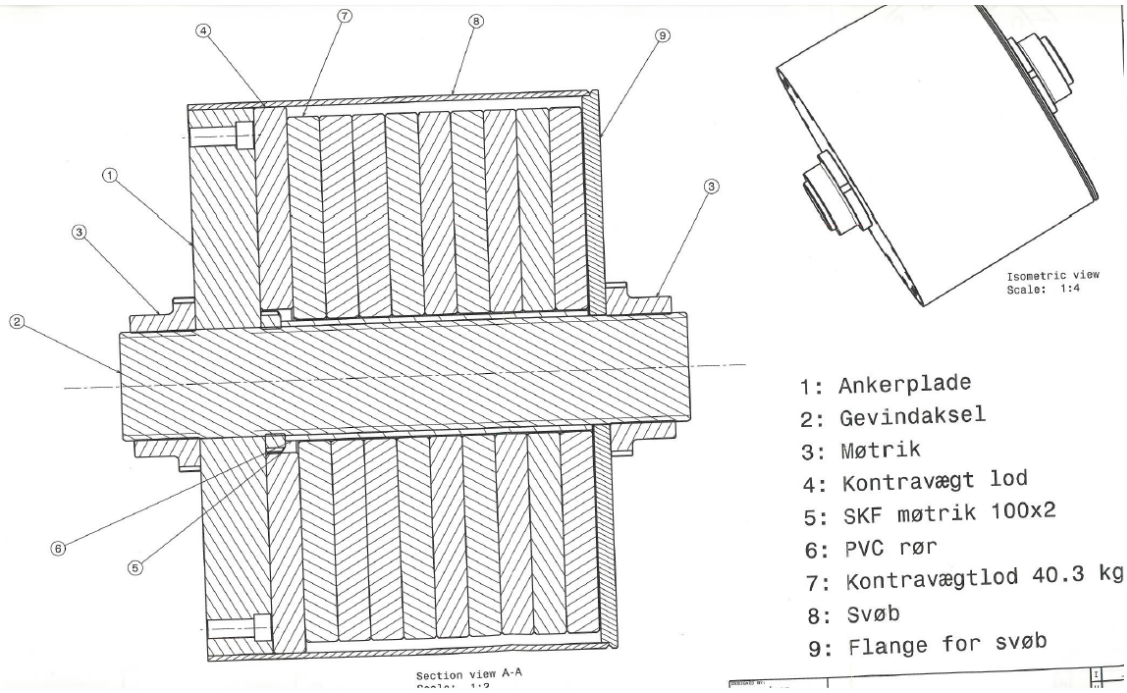

Figure 8 - Technical drawing of the third counter-weight section.

The list of the tubular section components comprising the counter-weight assembly is presented in **Table 2**, together with their characteristic parameters.

Table 2 - Counter-weight component parameters.

Part	Length [m]	Inner diameter [m]	Outer diameter [m]	Mass [kg]
Counter-weight section 1	1.970	0.2785	0.2985	140.34
Counter-weight section 2	1.070	0.500	0.520	134.30
Counter-weight section 3	0.620	N/A	N/A	538.38

Component design - hub

The hub assembly consists of the hub part, the frame which stores the pc and pitch drive and where the counterweight is connected, the pitch shaft for the boom, and the connection pieces and flanges between them (steel St52). The technical drawing of the hub assembly is shown in **Figure 9**. The list of the assumed tubular section components comprising the hub assembly is presented in **Table 3,** together with their characteristic parameters.

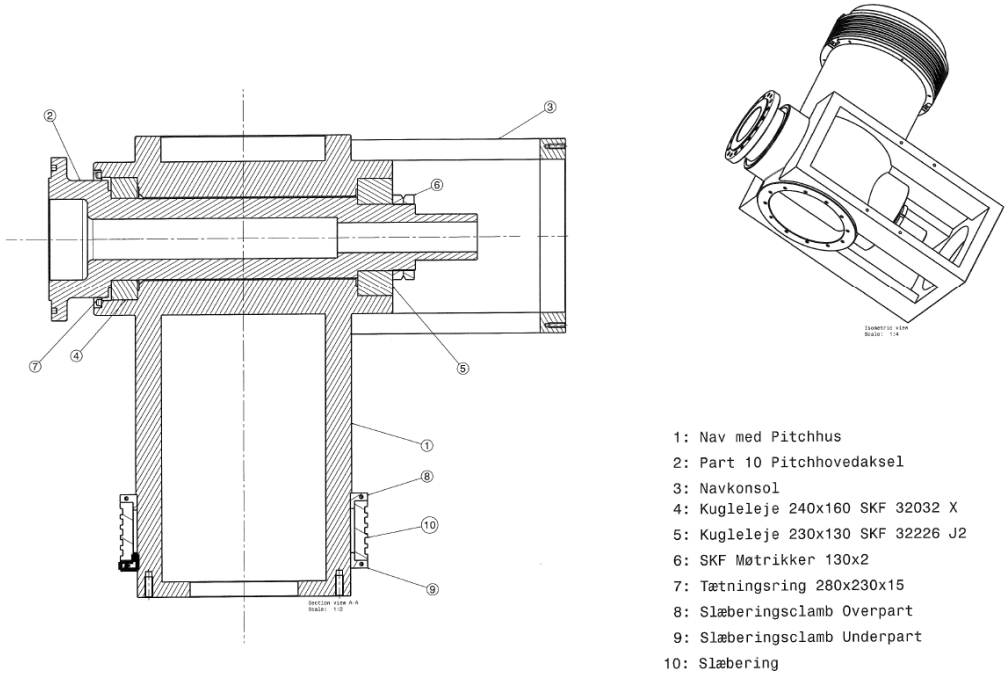

Figure 9 - Technical drawing of the hub assembly.

Table 3 - Hub component parameters.

Part	Length [m]	Inner diameter [m]	Outer diameter [m]	Mass [kg]
Hub part	0.900	0.319 (ref)	0.419 (ref)	550.00
Hub shaft	0.813	0.080 (ref)	0.158 (ref)	102.36

Final boom assembly

The boom assembly has been balanced using an artificial weight resembling the assumed weight of the wing as seen in **Figure 10**.

The total measured weight of the components of the full assembly is compared to the theoretical one from the CAD geometry in **Figure 11**.

Figure 10 - Balancing of the boom.

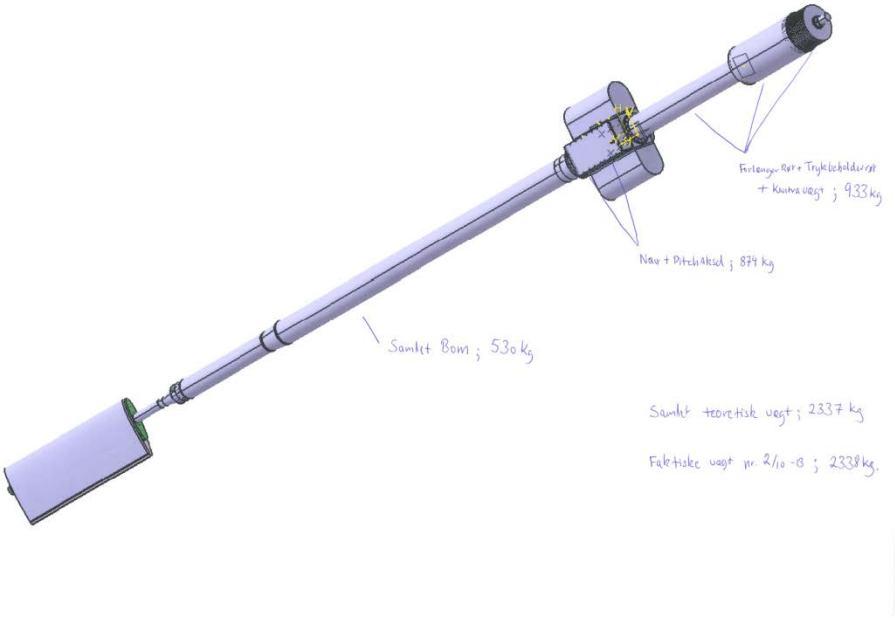

Figure 11 - Theoretical and measured weight of the assembly.

3. Pitch system design

In this section, the design of the pitch system for the rotating test rig is presented.

Pitch system assembly geometry
The system for pitching the boom consists of a linear actuator and a linkage structure, transferring the linear motion of the actuator to a rotation of the connecting base flange of the boom.

The pitch system location in the boom assembly is shown in **Figure 12**. The actuator and linkage structure are shown in a 3D view in **Figure 13**, and in drawing views in **Figure 14**.

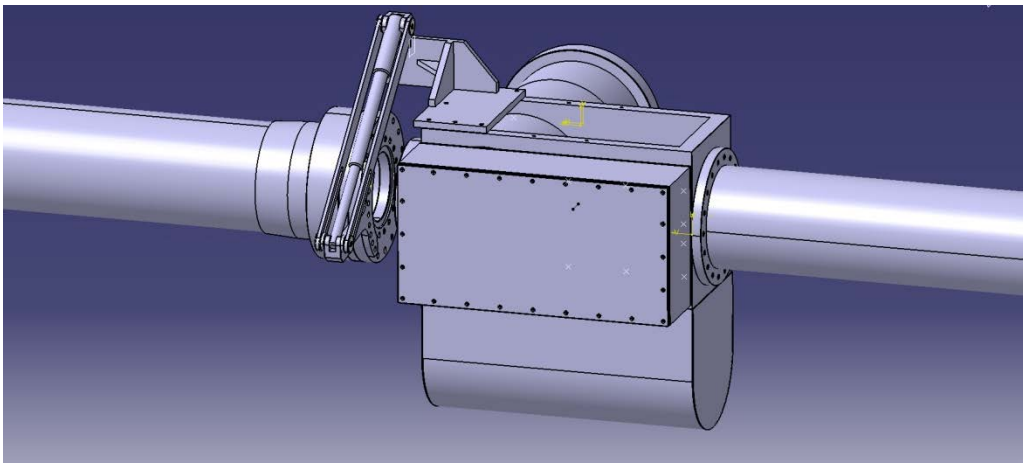

Figure 12 – 3D view of pitch system in boom assembly.

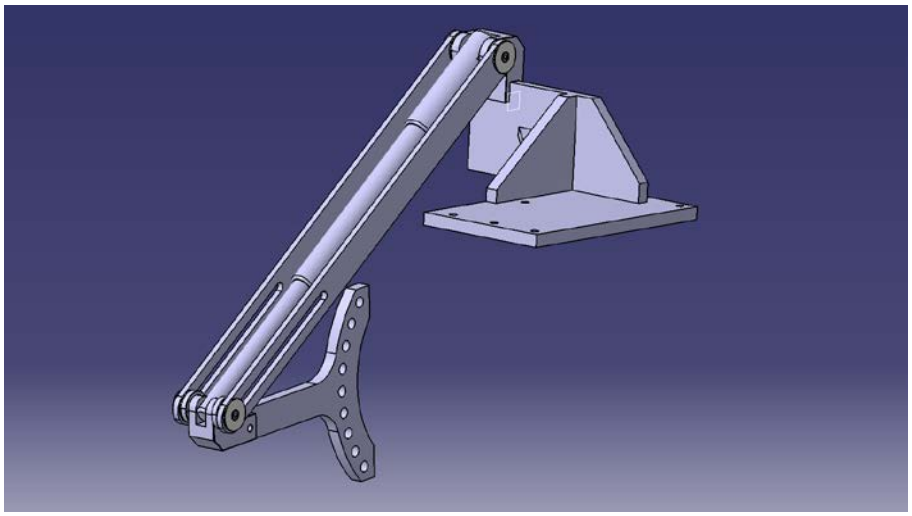

Figure 13 – 3D view of pitch system

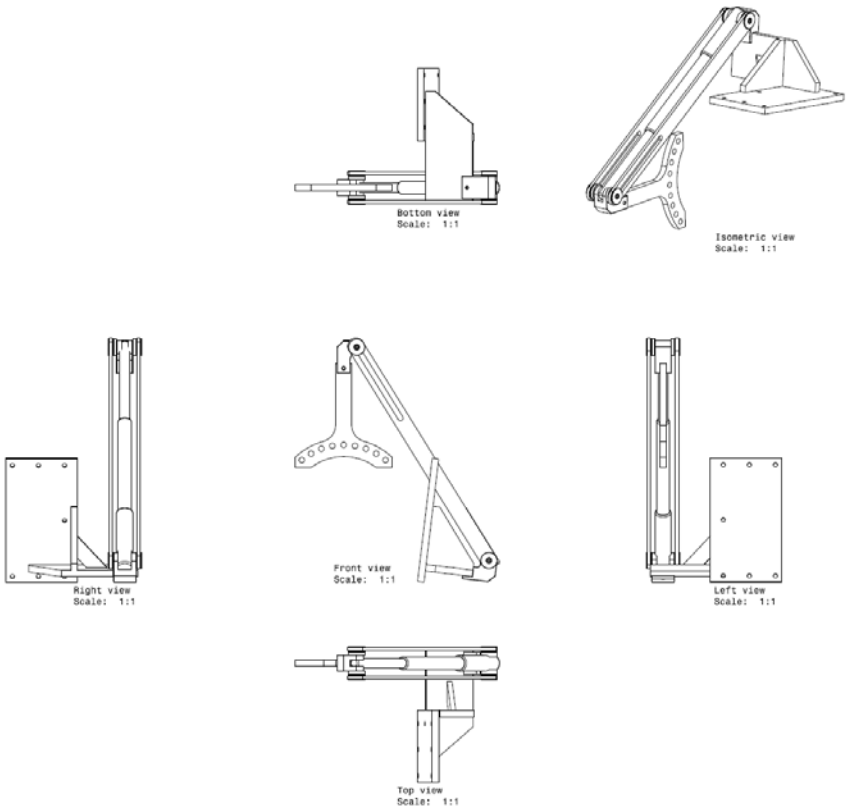

Figure 14 – Technical drawing of the pitch system.

The linear actuator is Concens Aktuator CON50, which has a stroke length of 250 mm, a blocking force of 4500N and a speed of 4 mm/s under maximum force. The main dimension and specifications of the actuator are shown in **Figure 15**.

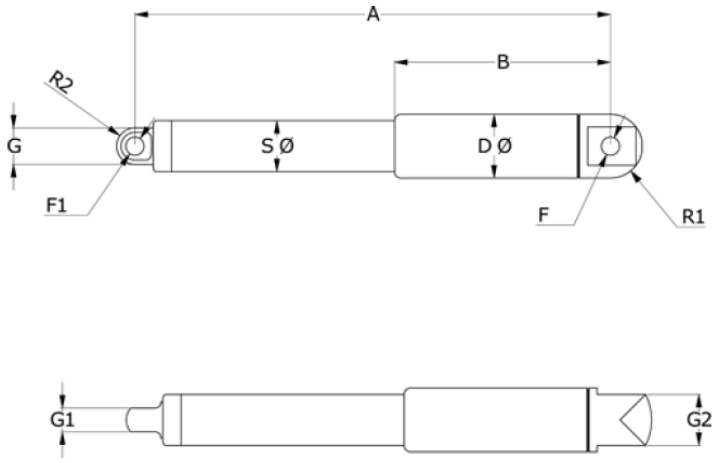

A	= 655
B	= 175
D	= 50
S	= 40
G	= 30
F1	= 16
F	= 16
R1	= 25
G1	= 20
G2	= 40
Vandring mm	= 400
Tryk (N)	= 4500
Hastighed ved maks.	= 4
belastning mm/sek	= 84
Udveksling	= 12 V
Spænding	= 1 mtr.
Kabellængde	

Figure 15 – Specifications of the linear actuator.

Based on the existing installation setup of the pitch system, the achievable pitch angle is in the range of 1 to 24.5 deg (pitch to stall in upwind configuration).

4. Electrical drive design

[Text]

[Headline]
[Text - The following line contains a section break - do not delete]

5. Blade section design and manufacturing

In this section, the design and manufacturing of the blade section for the rotating test rig is presented.

Wind turbine blade section concept

A wind turbine blade section based on the shape of a NACA0015 aerofoil has been manufactured with a constant chord length of 1 meter. Overall concept consists of a spanwise 2.2 meter long wing section covered with side pods in each end giving a total length of 3.4 meter. Wind turbine blade section is based on an inner aluminum structure covered with two shells of composite material. The aluminum structure consists of an ø110/100 tube, two spante structures and a U-profile web. Aluminum parts were welded together. The tube makes it possible to mount and dismount the wing section on a boom and the U-profile web at the trailing edge is for fixation of different morphing rubber flaps.

The section will among other things be equipped with three pressure tanks, valves, control units, data acquisition equipment, around 200 holes connected with individual rubber tubes for pressure measurement strategic places on the aerofoil. The main part of these holes are placed in the extended mid section of the blade where also the 5 liter pressure tanks are placed, see **Figure 16**. All parts have to be fixed in order to withstand impact from the centrifugal forces during operation.

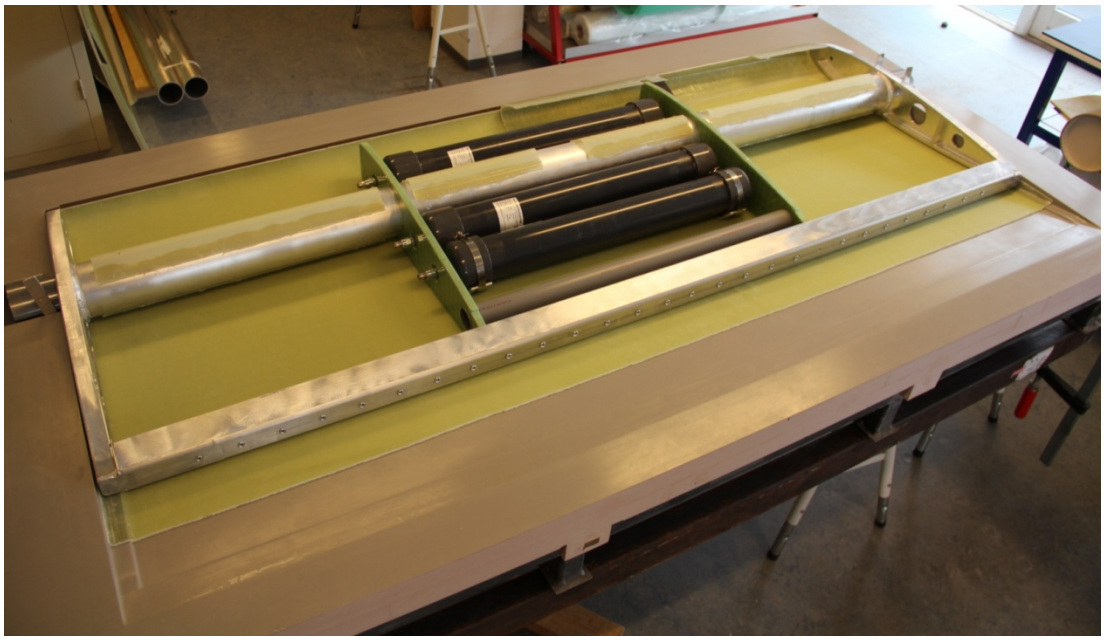

Figure 16 - Wind turbine blade section in the mold (light grey) seen from the trailing edge. On top of composite shell (green) is the welded aluminum structure and in the mid section pressure tanks.

The blade section is split in to three sections by two spante structures made of composite material. Three pressure tanks are placed in the mid section together with a tube (dark grey) for connection between the two outer sections. The blade mold was designed in such a way that it

was used for manufacture of composite shells and also used for alignment and glue assembling of the components**.**

Molds

Mold parts were manufactured by DENCAM (Fåborg, Denmark) based on drawing material from DTU Wind Energy. The moulds were designed with flanges necessary for vacuum bagging of the glass fiber material during vacuum infusion of the resin material. Furthermore were molds designed to allow alignment around the aluminum tube and assembly of wing components in the mold was possible. Vacuum tight molds were realized based on a foam material covered with layers of special paste for processing and grinding to final shape. NACA0015 blade profile is symmetric and possible to realize with only one mold part. Side pods were manufactured using two mold parts. Drawings of molds are shown in **Figure 17** and molds as delivered in **Figure 18**.

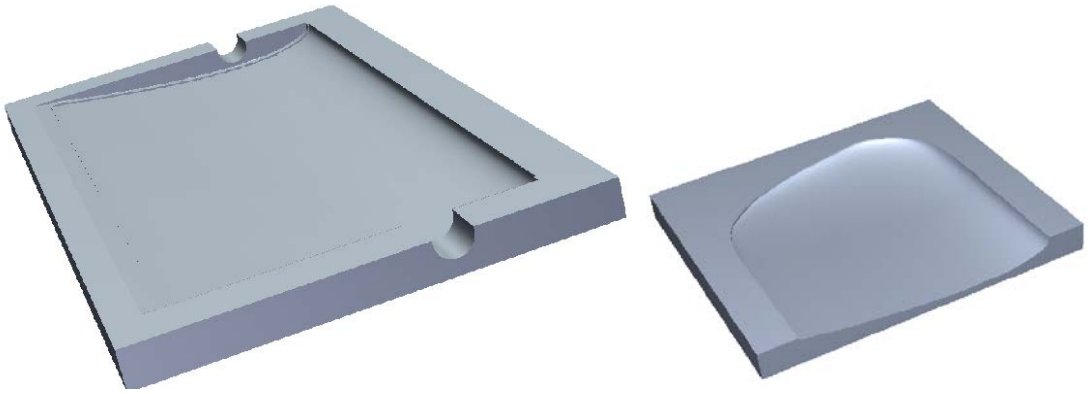

Figure 17 - Drawing of blade mold with flanges and tube alignment (left) and one of side pod molds (right).

Figure 18 - Delivered molds were cleaned and treated with a release agent; Zyvax Composite Shield delivered from Granudan (Stenløse, Denmark) and later on REXCO´s wax PARTALL #2 delivered from R&G Faserverbundwerkstoffe GmbH (Waldenbuch, Germany).

Manufacture of composite shells and assembly

Two types of glass fiber fabric from SAERTEX (Saerbeck, Germany) were used for the composite parts:

- Stitched Unidirectional (UD) fabric, area weight 1186 g/m^2
- Stitched ±45° BIAX fabric, area weight 450 g/m^2

Resin infusion system, gelcoat and adhesive were delivered from HF Industri & Marine (Svenborg, Denmark):

- Epoxy resin/hardener: PRO-SET 117/226PF, mix ratio 100/34 by weight. Mixed viscosity at 25°C 440 mPas
- Gelcoat: PRO-SET 364 White, epoxy
- Adhesive: PRO-SET 170

To obtain a white surface color of the laminate, white gelcoat was first applied in the mold. The gelcoat was applied as two single layers with a cure time in between to ensure a thin and uniform surface layer.

Most of the wing shell laminate lay-up was established using a 6 layer lay-up: [+-45, 0, 90, 90, 0, +-45]. To increase the laminate thickness in the overlap area between wing section and side pod an extra 0° layer was added giving a lay-up: [+-45, 0, 90, 0, 90, 0, +-45]. Gelcoat in mold and glass fiber lay-up is shown in **Figure 19**.

Figure 19 - Side pod mold with applied gelcoat (left) and lay-up of glass fabric on top of gelcoat (right).

Vacuum bagging of the lay-up for vacuum infusion was established using “standard” bagging materials mostly delivered from Airtech Europe (Diffeerdanger, Luxembourg):

- Peel-ply release: Release Ply A
- Low profile resin distribution medium: Greenflow 75
- Flexible nylon bagging film: Stretchlon® 800
- Sealant tape: GS 213

- PTFE pressure sensitive tape: Teflease MG2
- Connection to resin trap/vacuum and resin pot: Nylon barb "T" fittings
- Connection to resin trap/vacuum and resin pot: Nylon tubing 1/2"
- Resin outlet manifold: Nylon spiral tubing

For resin inlet manifold Enka-Channel 50 from COLBOND (Arnhem, Netherlands) was used. Vacuum bagged side pod is shown in **Figure 20** and **Figure 21** shows the flow front during the vacuum infusion.

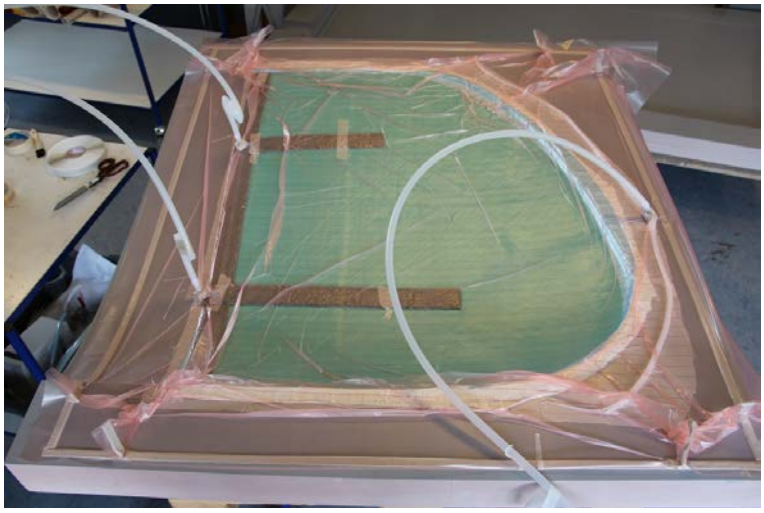

Figure 20 - Vacuum bagging of side pod.

Two nylon tubes for resin inlet on the left side in **Figure 20** were connected through the sealed vacuum bag to the resin manifold, who acts as a “highway” for the resin during infusion. The green distribution net cover almost the entire laminate and only a small “break zone” is used between lay-up and resin outlet manifold on the right side, where the tube is connected to the resin trap/vacuum pump. Sealing of the vacuum bag is performed on the mold flange by the tacky sealant tape.

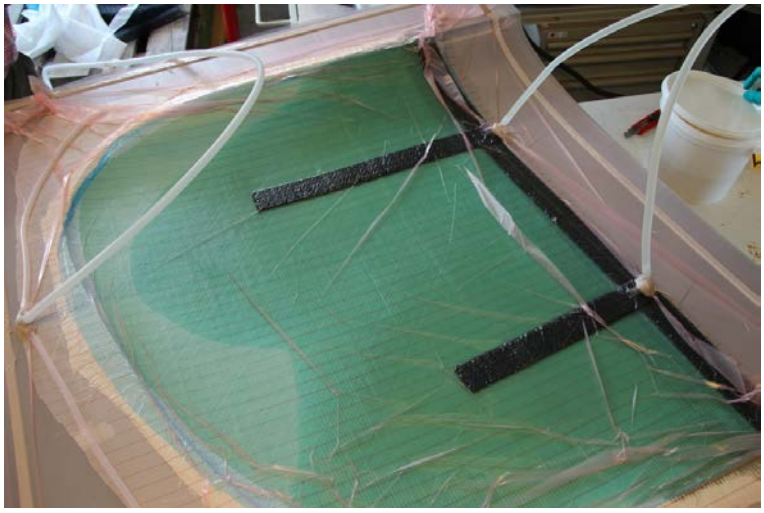

Figure 21 - Vacuum infusion of a side pod. The resin pot can be seen in the top right corner. Approximately ⅔ of the glass fiber lay-up is wetted out; this can be seen as the color change (becoming darker) through the vacuum bag.

When the entire glass fiber lay-up was wetted out and some resin had reached the outlet tube, the two inlet tubes were closed and vacuum outlet kept open at a reduced vacuum level, typically 60% of the vacuum level used during infusion. The resin was cured over night, 16 hours, with maintained vacuum pressure and reached a brittle “B” stage after 24 hours at room temperature. Post cure was performed at 50°C for 16 hours in the mold with a heat blanket before demolding.

Edges of side pods laminates was trimmed to the wanted size and the shells were glued together along the edge fixated in one of the molds, as can be seen in **Figure 22**. Subsequently the bondline was grinded and excess adhesive removed from the outside. Strengthening of the bondline at the inside was performed manually using layers of the BIAX ±45 fabric for over lamination.

Tip side pod has a spanwise length of 0.7 meter where the first 0.2 meter also has the NACA0015 airfoli profile in order to ensure enough space for electrical and pressure connections coming from the nacelle through the boom and into the wing section through holes in the outer aluminum spante. The inner side pod is 0.5 meter long and without the 0.2 meter NACA0015 airfoil profile. Geometry of the hole for the expected boom design in the inner side pod was marked by a “scratch” in the mold. This concept worked well in practice and the hole was cut using the guideline from the "scratch". The dimensions of the boom were increased for safety reasons and the inner side pod had to be split in to two parts which can be mounted directly on the boom. Manufactured side pods are shown in **Figure 23**.

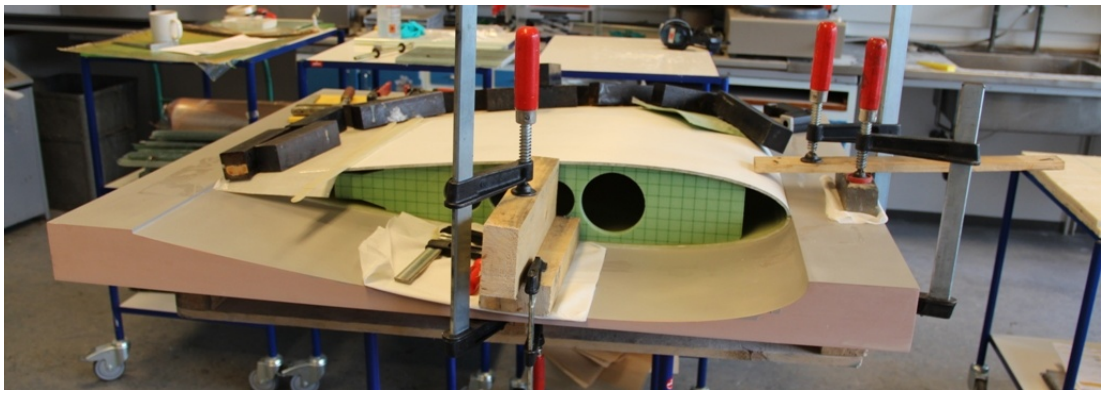

Figure 22 - Assembly of a side pod from two composite shells in one of the molds.

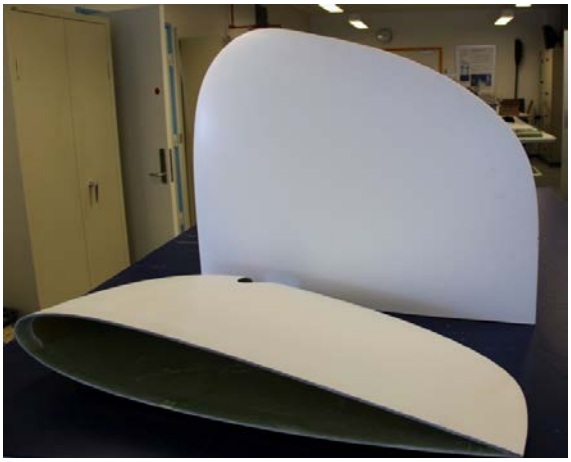

Figure 23 - Manufactured side pods with a length of 0.7 meter and 0.5 meter respectively.

The composite shells for the wing section were manufactured in accordance with the side pod shells. The resin inlets were placed down the center of the section with outlet along both leading and trailing edge, whereby the flow distance of the resin was reduced to less than 60 cm. Four rectangular hatches from a pre consolidated laminate were cut to the wanted size, wrapped in a thin release foil and placed in the mould at the wanted predefined locations. Glass fiber layup was placed over the entire area and also on top of the hatches before vacuum bagging and resin infusion, whereby space for the hatches was casted into the laminate structure with a perfect fit. Pictures from the manufacture of the shell laminate with hatches can be seen in **Figure 24** and **Figure 25**.

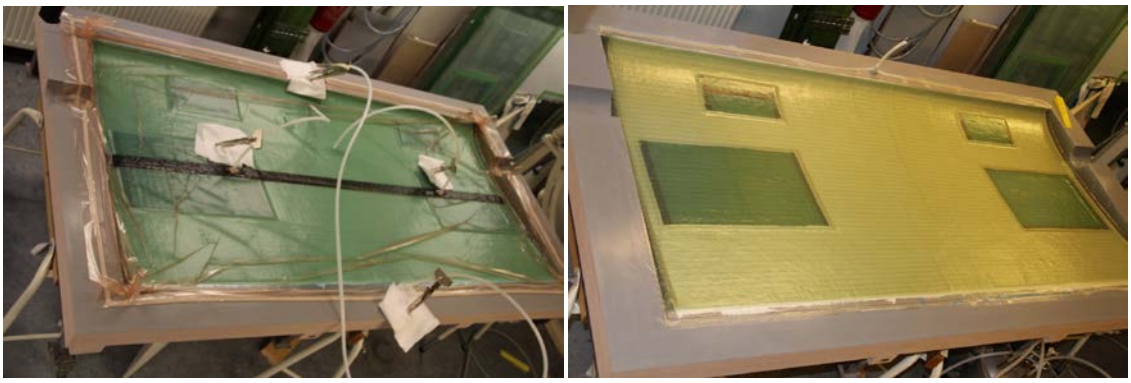

Figure 24 – Left: Vacuum infusion of wing shell with hatches placed in the mold. Resin inlet is placed in the center and outlet is established along both the leading and trailing edge. Right: Cured wing shell in mold before demolding

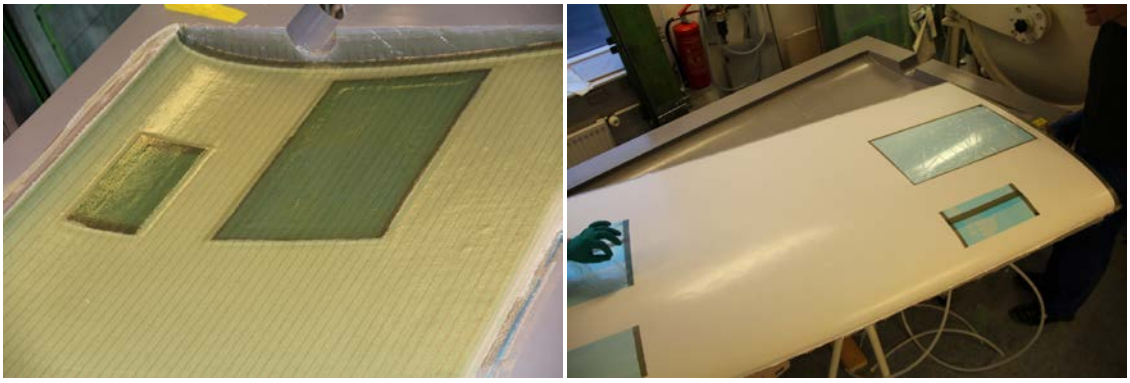

Figure 25 – Right: Close up of hatches casted into the laminate in order to obtain perfect fit. The holes for the hatches were cut afterwards. Right: Hatches covered with release foil were carefully removed and labelled.

Preparation of composite shells before assembly of wing section

Before the wing shells where bonded together several actions were performed in order to ease the job in a rational way. For pressure measurements, especially in the mid section, holes placed in a specified pattern to avoid that measurements conflict with each other were drilled. In each hole was a stainless steel tube first fixated with fast curing (seconds) cyanoacrylate adhesive in a position, where the end of the tube was in level with the outer surface of the wing laminate. Subsequently were the steel tubes further fixated and supported by an epoxy adhesive, Scotch Weld DP460 from 3M. This is illustrated in **Figure 26**.

Figure 26 - Pressure holes were drilled in the shell at specific locations. Stainless steel rods were mounted with first cyanoacrylate and subsequently by an epoxy adhesive.

Rubber tubes of equal length were labeled and connected to the tubes. The length of the tubes was equal to ensure the same time delay of the measurements. The excess length of the tubes has to be fixated inside the blade section. To avoid conflict with the bondline areas were the tubes fixated to the laminate shell with a tough black silicone rubber adhesive, see **Figure 27**.
Preparation of the welded aluminum part involved first cleaning and removal of lubricant from the machining. A glass fiber composite V-profile was manufactured in lengths of approximately 1 meter and glued to the aluminum tube. The V-profile provides the necessary contact between the wing shell and the aluminum tube and was mounted using PRO-SET 170 adhesive. The V-profiles can be seen in **Figure 28**. For overlap and reinforcement of the bondline at the leading edge were two U-profiles matching the inner geometry of the wing manufactured in a separate mold and glued to the composite shell with the hatches using PRO-SET 170 adhesive. Placement of overlap and removal of excess adhesive at leading edge is shown in **Figure 29**, where also the special hangers for fixation of pressure tanks by clamp bands can be seen.

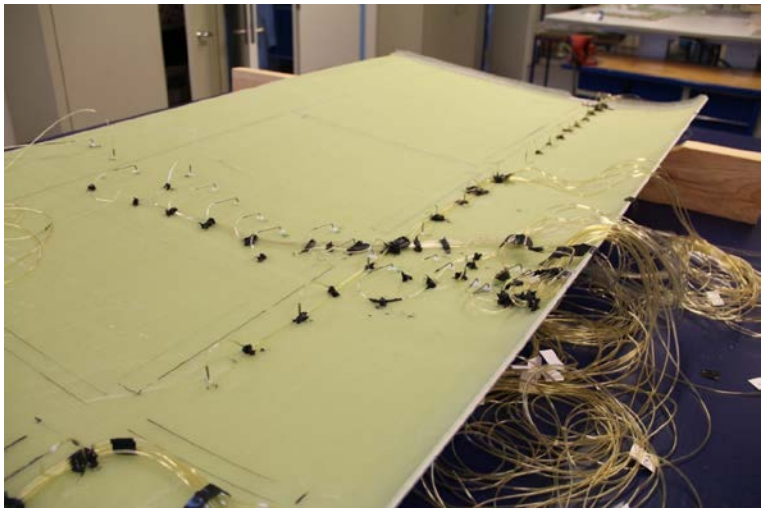

Figure 27 - Each tube was connected with a rubber tube of equal length to ensure the same time delay of the measurements and all tubes were fixated to the composite shell by silicone adhesive.

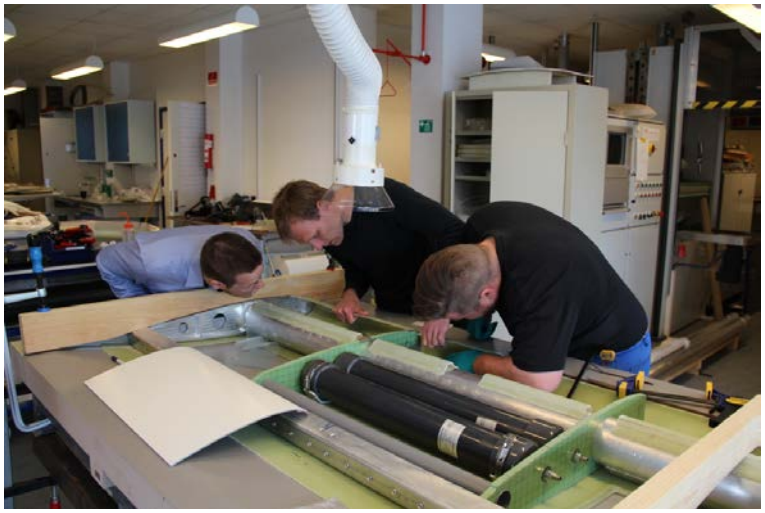

Figure 28 - Mounted V-profiles on top of the aluminum tube. Position of bondlines were marked together with positions of the U-profile overlap at the leading edge.

Figure 29 – Left: U-profile overlap mounted at leading edge on the shell structure with hatches. Right: Removal of excess adhesive from the bonding of the leading edge overlap.

Bondline areas were cleaned prior to bonding. Aluminum surfaces were lightly scratched and cleaned again in order to obtain a good bond. PRO-SET 170 adhesive was applied using a glue gun and afterwards manually spread out before carefully placement of the aluminium structure. Bondline thickness was obtained using spacers glued to the laminate at selected points.
The aluminium structure was aligned in the mold by the special design of the tube support in each end and clamped towards the mold using a wood beam prepared with the wing profile. Excess adhesive was removed when the aluminium structure was in place. Bonding of the aluminium structure to the composite shell is documented in **Figure 30**.

Following the first assembly an extra tube connection through the mid-section was established and pressure tanks mounted and fixated. **Figure 31, Figure 32,** and **Figure 33** show details of the mid-section before the second assembly; over lamination of spante, fasteners for later fixation of tubes glued in strategically points and pressure tanks connections available through holes in spante.

Figure 30 – Left: Preparation of aluminium part. Right: Placement of adhesive in the marked bond lines using a glue gun.

Figure 31 – Left:The adhesive was manually spread out before placement of the aluminium structure. Right: Carefully placement of aluminium structure on top of composite shell.

Figure 32 – Left: Fixation of aluminium structure. Bondline thickness was obtained using spacers. Right: Aluminium structure was aligned in the mold by the special design of the tube support in each end. Excess adhesive was removed when the structure was in place.

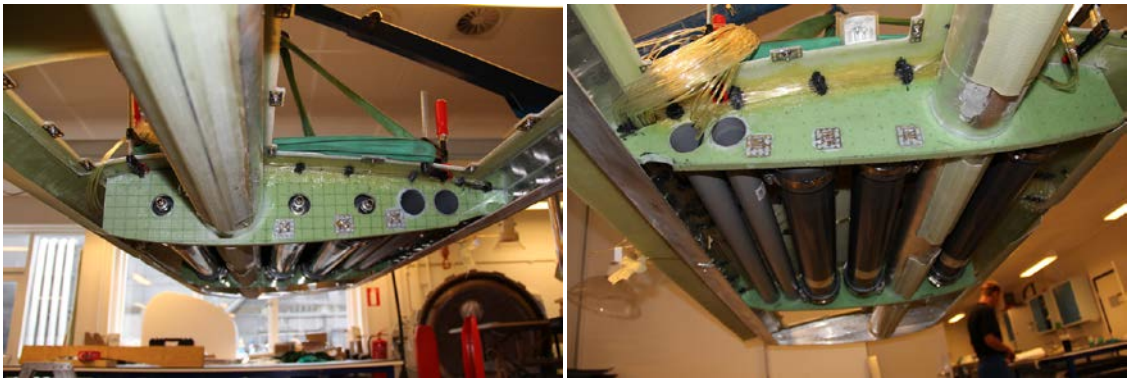

Figure 33 – Left: Details in mid section before assembly. View towards tip. Right. Pressure tanks in position and clamp band fixated with glue. View towards hub.

Leading edges of the composite shells were machined to fit each other, **Figure 34**, and the hatches were also trimmed, **Figure 35**, to obtain as much space as possible. Sealing of the hatches was obtained by casting a silicone ribbon in a groove along the edge.

Figure 34 - Trimming of leading edge before assembly using a high speed drill .

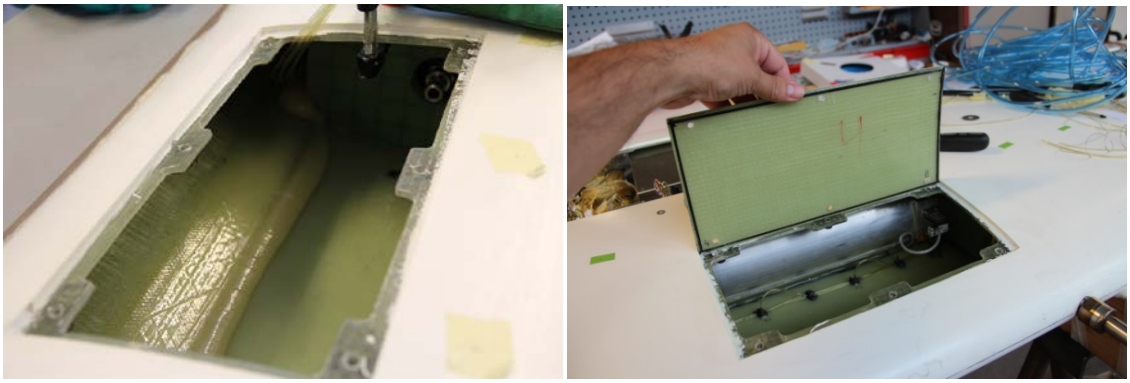

Figure 35 - Tooling of the flange for the hatches in order to obtain as much open space as possible. Fasteners with nuts were glued in position. Sealing of the hatches was obtained by casting a silicone ribbon, seen as black line, in a groove along the edge.

Fit between components were checked prior to bonding and also the connection for each of the mounted pressure channels, illustrated in **Figure 36**.

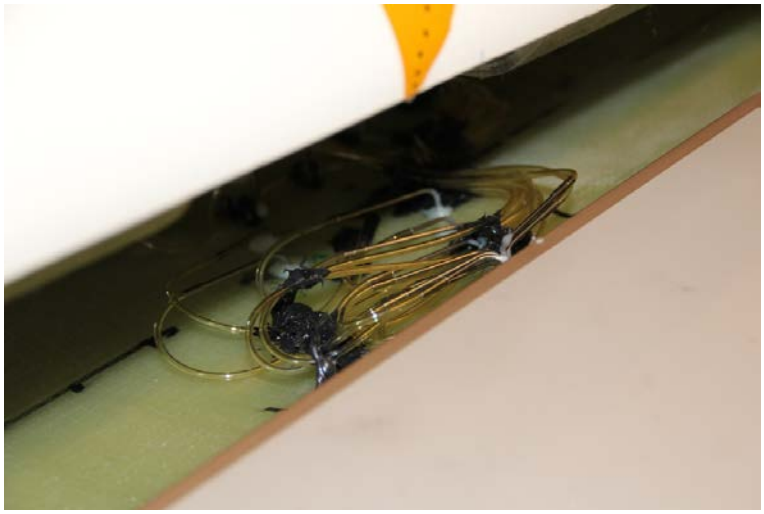

Figure 36 - Check of space and test of pressure tubes - all work before assembly.

Second assembly of wing shells is documented in **Figure 37**, **Figure 38**, and **Figure 39.** The procedure was very similar to the first assembly, but more difficult due to less space, restricted access and the fact that all subsequent processing had to be performed through the hatches.

Figure 37 – Left: Adhesive being spread out in the marked bondline areas of the shell placed in the mold. Right: Top part mounted in a portable crane for easy and controlled joining of the parts.

Figure 38 - Tube steering was used for fixation of components during assembly.

Figure 39 – Left: Removal of excess adhesive. Right: Pressure holes were covered with tape during the bonding to prevent them from being blocked.

The final preparation of the wind turbine blade involved cutting of the trailing edge in order to get the wanted 50mm distance between U-profile and shell laminate edge, **Figure 40**, and mounting of side pods. Holes for pitot tubes in the leading edge were drilled, **Figure 41** and the total weight of the composite structure measured to 96 kg.

Figure 40 - Left: Laser lineup of laminate before cutting of trailing edge. Right: Mounting of side pods to wing section using helicoils in the aluminum spante. Good fit between wing section, side pods and hatches.

Figure 41 – Left: Holes for mounting of pitot tubes in leading edge. Right: Blade section with mounted side pods had a total weight of 96 kg before devices and rubber trailing edge was mounted.

Observations and recommendations for future manufacture of wing sections
This section summarizes some of the lessons learned during manufacture of the blade section.

- Good fit between manufactured composite components (**Figure 42**).

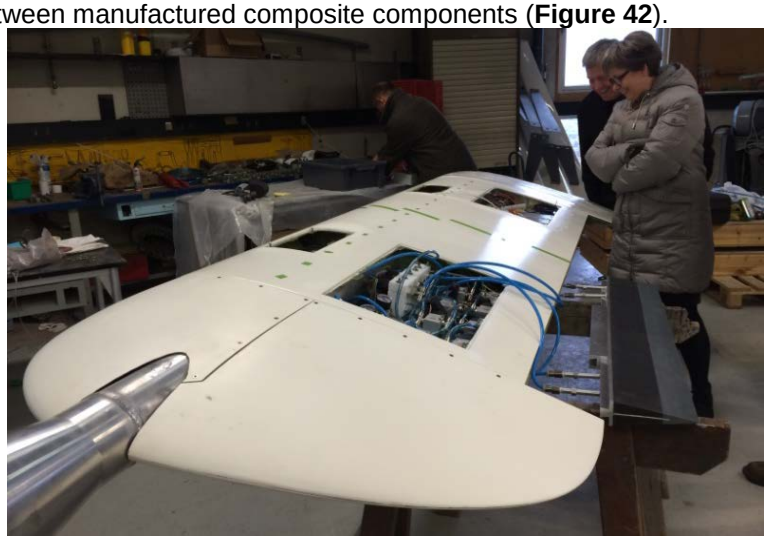

Figure 42 – Blade section mounted on boom.

- The use of molds for both lay-up and consolidation of composite material as well as alignment and assembly of sub structures has worked well.
- Tube for alignment of blade structure worked well.
- Material system, glass/epoxy system PRO-SET 117/226PF, works well. Fast delivery in relative small quantity. Good material quality was obtained by vacuum infusion.
- Gel-coat (PRO-SET 364 White) and adhesive (PRO-SET 170) works well.
- Perfect fit of hatches in the blade structure was obtained.
- Mark up of the hole (by a scratch in the mold) to be cut in inner side pod worked well
- Trailing edge design. It was difficult to realize the wanted dimensions and perfect fit between blade section and rubber part. The position of the U-profile has to fit the distance to the composite trailing edge and at the same time the height of the blade profile and the angels of the blade shells. An improved design was realized building a 2m long blade section for lightning test and also used for realized demonstrators. This concept is shown in **Figure 43**.

Figure 43 – Blade section mounted on boom.

6. Instrumentation

In this section, the instrumentation of the rotating test rig components is presented, as utilized in the measurement campaign of the INDUFLAP project.

Overview of instrumentation, sensors and control hardware

The overview of the sensors and signal connections in all components of the rotating rig is shown in **Figure 44**.

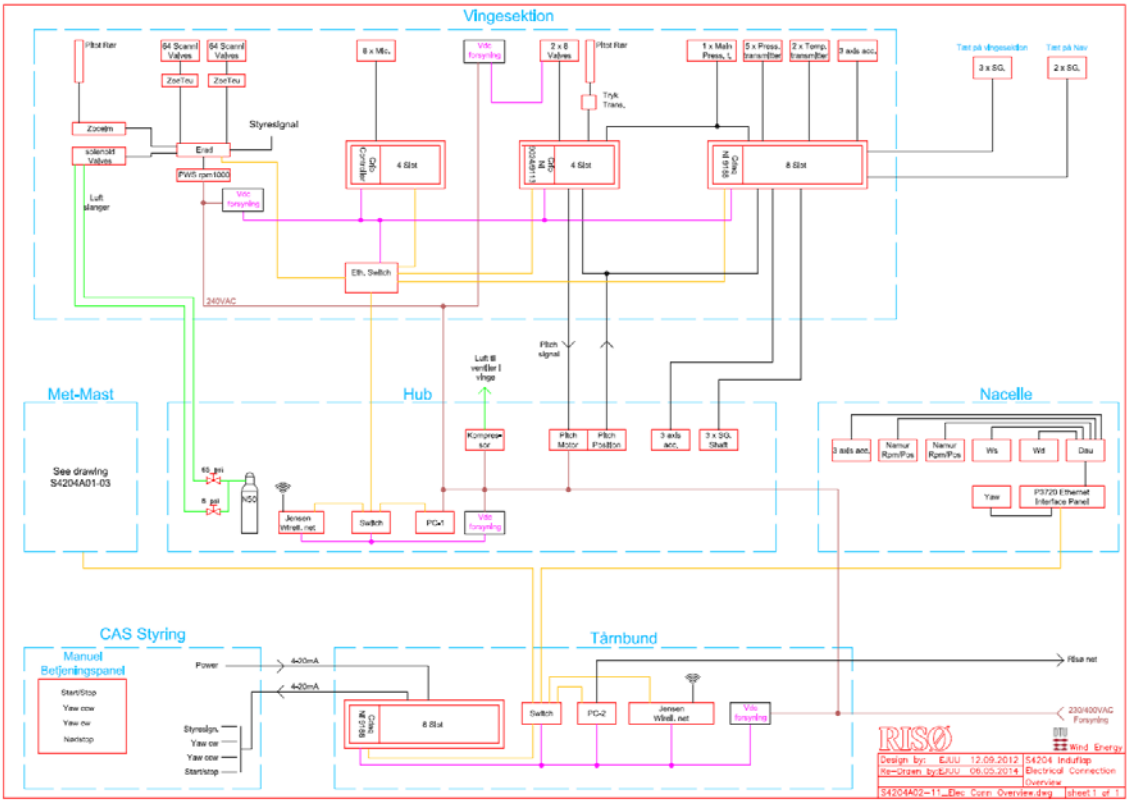

Figure 44 – Instrumentation overview.

A list of sensors per main component is presented below:

<u>Blade section:</u>

- 2x64 Scani-valve pressure taps
- 2 5-hole Pitot tubes
- 1 3-axis accelerometer
- 3 strain gauges
- 2 command pressure signals for flap
- 3 pressure switch signals (low, mid, high) for flap
- 1 main pressure supply signal for flap
- 2 temperature transmitters

Boom:

- 2 strain gauges

Hub:

- 3 3-axis accelerometer
- 3 strain gauges on shaft
- Pitch position
- Pitch command signal

Nacelle:

- 1 3-axis accelerometer
- Shaft position/rpm sensor
- Wind speed at 3 heights (from met mast)
- Wind direction at 3 heights (from met mast)
- Yaw position

The overview of the sensors and signal connections in the wing section is shown in **Figure 45**.

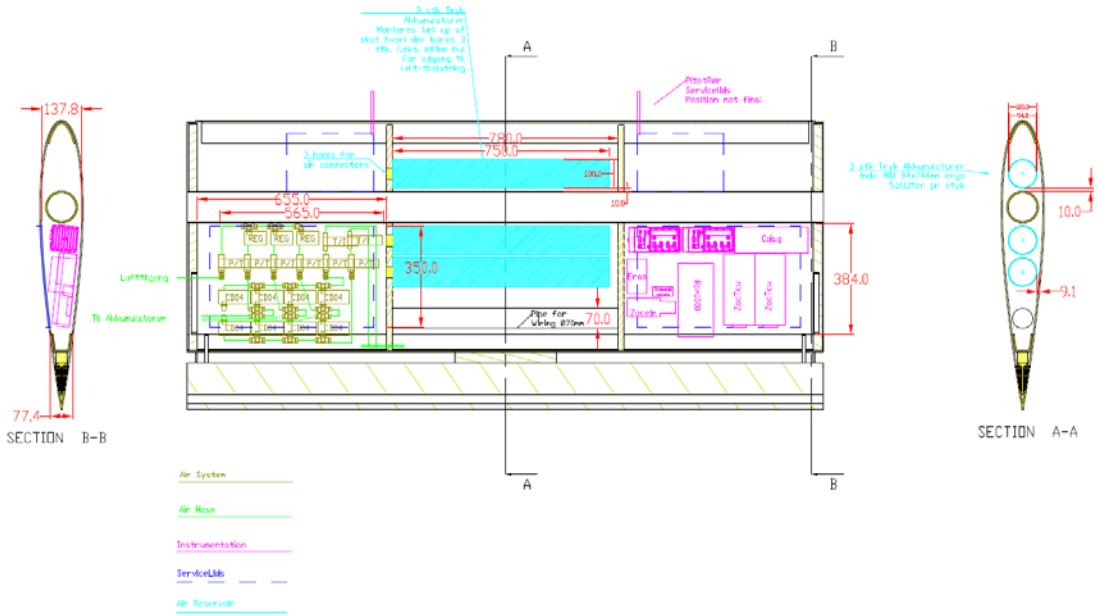

Figure 45 – Instrumentation on the wing section.

The controller hardware consists of a real-time controller (cRio NI 9024/9113) and two data acquisition systems (cDAQ NI 9188) from National Instruments. The cRio controller is used to control the flap and pitch systems, while one of the cDAQ systems is used for signal monitoring, both located in the wing section. The pc accessing the two controllers is located in the pc-box on the hub. The second cDAQ system is located at the tower bottom and it is used to control the turbine. Tests of the controllers are made through a Labview graphical interface running on the mini PCs.

Flap system details and calibration

The flap powering system, which is developed and implemented by Hydratech Industries, comprises a pneumatic system providing pressurized air into the voids of the flexible part of the flaps. A compressor supplies pressurized air into 3 accumulators, where the pressure is regulated through regulator valves into low, medium, and high pressure. A series of 3 switches per flap side ('positive'-upper, 'negative'-lower) control which of the three pressure levels is connected to the flap voids (on-off). A forth switch per flap side controls the release of pressure. Controlling the switch valves allows for dynamic control of the pressure in the voids and therefore the flap deflection. The pressure at the flap inlets, the switches, the accumulators and the compressor are measured using pressure transducers. The schematic of the power system lines and connections is shown in **Figure 46**. The implemented switches and transducers in the test section are shown in **Figure 47**.

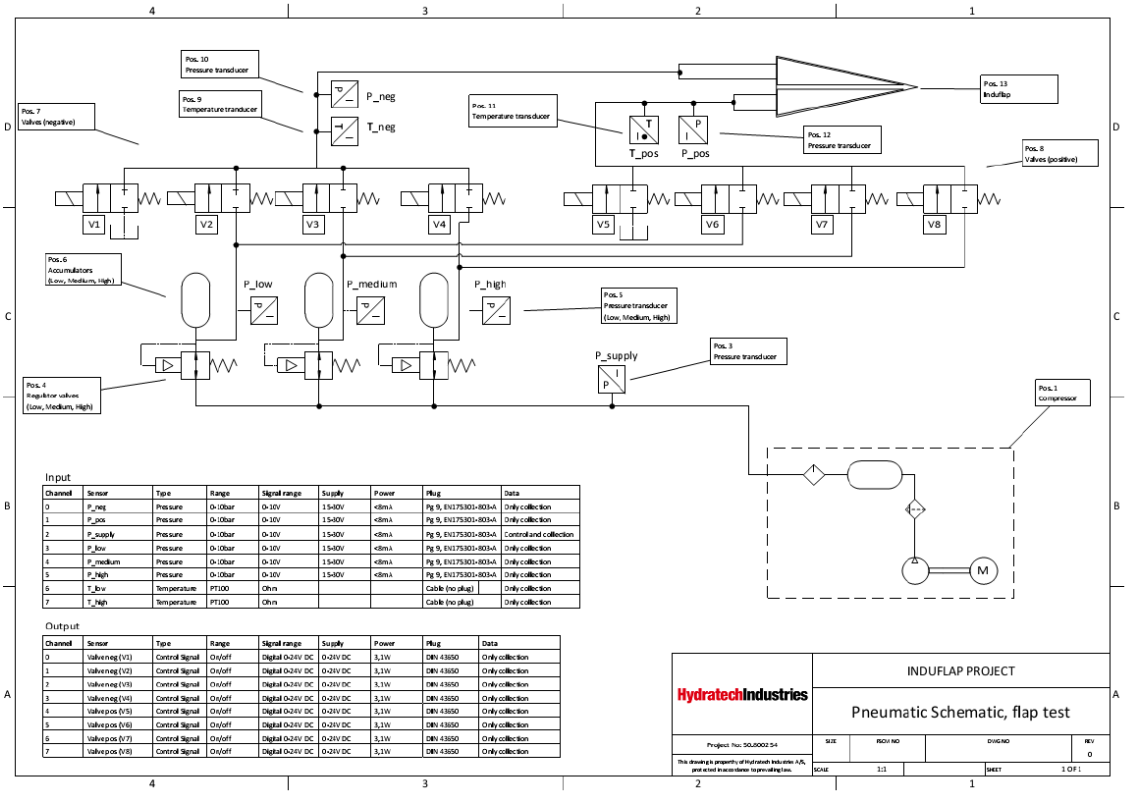

Input								
Channel	Sensor	Type	Range	Signal range	Supply	Power	Plug	Data
0	P_neg	Pressure	0-10bar	0-10V	15-30V	<8mA	Pg 9, EN175301-803-A	Only collection
1	P_pos	Pressure	0-10bar	0-10V	15-30V	<8mA	Pg 9, EN175301-803-A	Only collection
2	P_supply	Pressure	0-10bar	0-10V	15-30V	<8mA	Pg 9, EN175301-803-A	Controll and collection
3	P_low	Pressure	0-10bar	0-10V	15-30V	<8mA	Pg 9, EN175301-803-A	Only collection
4	P_medium	Pressure	0-10bar	0-10V	15-30V	<8mA	Pg 9, EN175301-803-A	Only collection
5	P_high	Pressure	0-10bar	0-10V	15-30V	<8mA	Pg 9, EN175301-803-A	Only collection
6	T_low	Temperature	PT100	Ohm			Cable (no plug)	Only collection
7	T_high	Temperature	PT100	Ohm			Cable (no plug)	Only collection

Output								
Channel	Sensor	Type	Range	Signal range	Supply	Power	Plug	Data
0	Valve neg (V1)	Control Signal	On/off	Digital 0-24V DC	0-24V DC	3,1W	DIN 43650	Only collection
1	Valve neg (V2)	Control Signal	On/off	Digital 0-24V DC	0-24V DC	3,1W	DIN 43650	Only collection
2	Valve neg (V3)	Control Signal	On/off	Digital 0-24V DC	0-24V DC	3,1W	DIN 43650	Only collection
3	Valve neg (V4)	Control Signal	On/off	Digital 0-24V DC	0-24V DC	3,1W	DIN 43650	Only collection
4	Valve pos (V5)	Control Signal	On/off	Digital 0-24V DC	0-24V DC	3,1W	DIN 43650	Only collection
5	Valve pos (V6)	Control Signal	On/off	Digital 0-24V DC	0-24V DC	3,1W	DIN 43650	Only collection
6	Valve pos (V7)	Control Signal	On/off	Digital 0-24V DC	0-24V DC	3,1W	DIN 43650	Only collection
7	Valve pos (V8)	Control Signal	On/off	Digital 0-24V DC	0-24V DC	3,1W	DIN 43650	Only collection

Figure 46 – Schematic of the flap powering system.

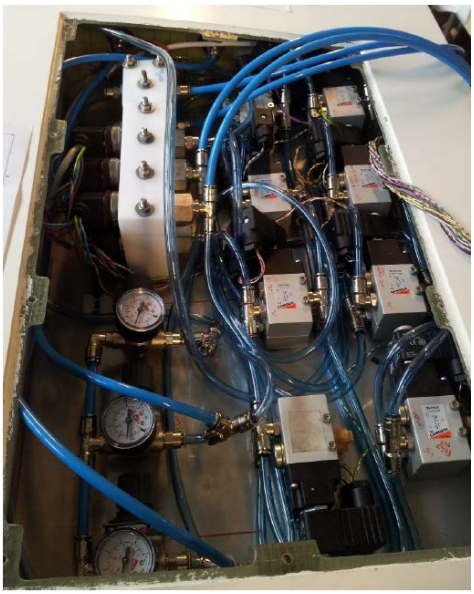

Figure 47 – Pressure switches and transducers implementation in the test section.

The calibration of the flap deflection has been performed on 16/10-2013, using the setup shown in **Figure 48**, where the inlet pressure and trailing edge deflection are monitored, using pressure transducers and a laser position sensor.

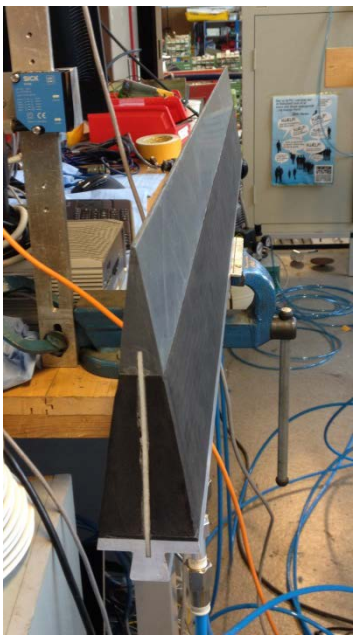

Figure 48 – Flap calibration setup.

A series of flap square command signals are used, and the pressure at the flap inlets ('positive'-upper, 'negative'-lower) is measured, together with the position of the flap trailing edge. The captured data is shown in **Figure 49** and **Figure 50**.

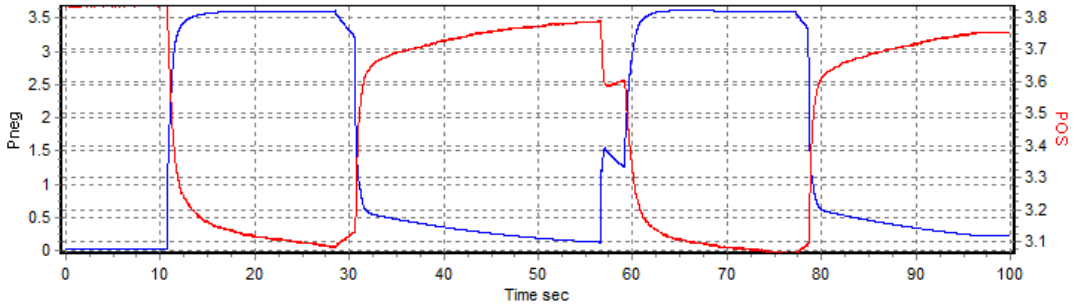

Figure 49 – Calibration flap deflection using of negative (lower) flap pressure. P_{neg}: Pressure in lower part of the flap. POS: Position of flap trailing edge.

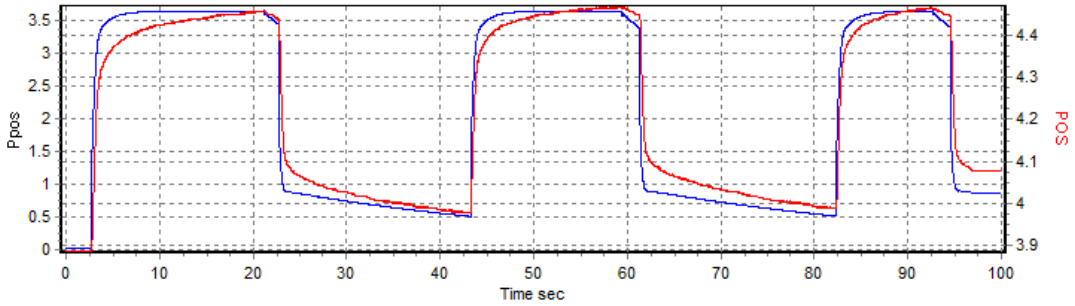

Figure 50 – Calibration flap deflection using of positive (upper) flap pressure. P_{pos}: Pressure in upper part of the flap. POS: Position of flap trailing edge.

The resulting flap calibration data is shown in **Table 4**.

Table 4 - Flap calibration data

	flap pressure [bar]	flap trailing edge deflection / pressure [mm/bar]	flap angle / pressure [deg/bar]
positive	3.6	4.86	1.85
negative	3.6	3.88	1.48

The flap angle is defined by the rotation of the flap trailing edge with respect to the flap hinge point and is calculated by the inverse tangent of the flap trailing edge deflection over the distance to the hinge point (0.15m).

Pitot tubes details and calibration

The Pitot tubes used from Aeroprobe USA have 5 ports and a static ring, and two air pressure gage transducers are connected to the P16 and P45 pressure sensors with a 0-1 psi range as shown in **Figure 51**. The 'pitch' angle α (**Figure 52**) is used as a measure of the local flow angle. The P1-P6 (where P6 is the static ring pressure) and P4-P5 pressure differences are utilized in order to determine the relative velocity and local flow angle. The position and numbering of the holes is shown in **Figure 53**. The serial numbers of the Pitot tubes used are:

- C07-70-1 (outboard tube – 'tip')
- C07-70-2 (inboard tube – 'rod')

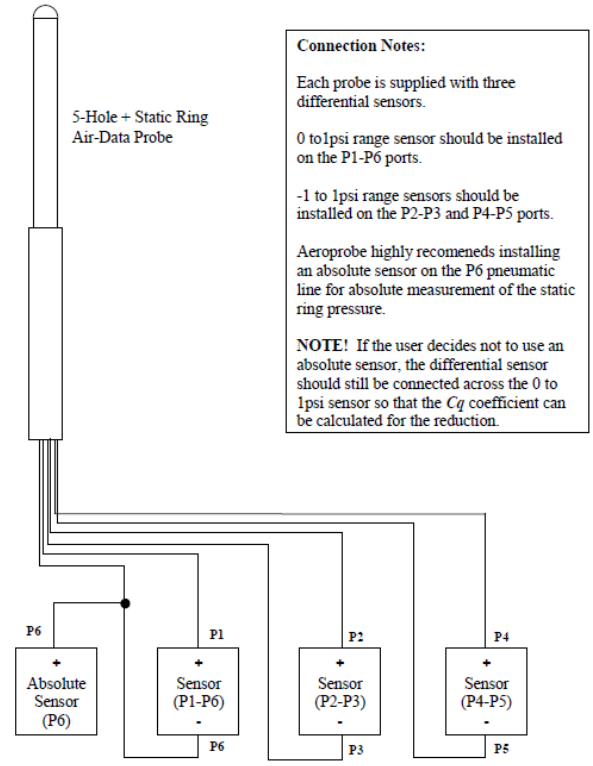

Figure 51 – Pitot tube sensor signals.

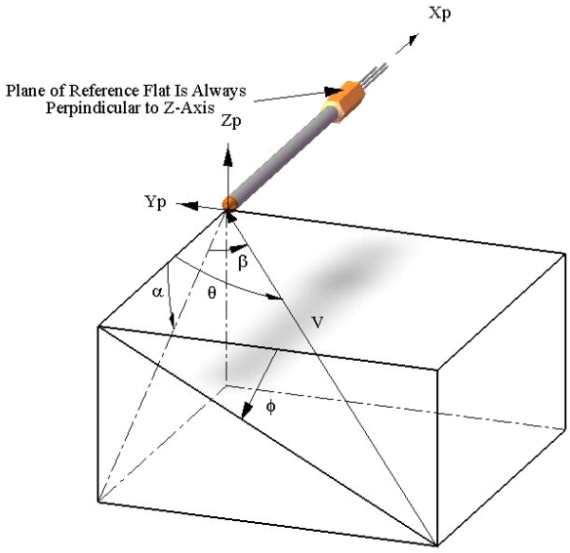

Figure 52 – Definition of measured flow angles using the Pitot tube.

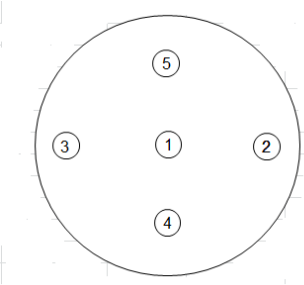

Figure 53 – Definition of pressure hole numbers in the Pitot tube.

The calibration of the Pitot tubes has been carried out by AeroProbe and is documented in a number of Excel sheets. The same tubes have been used in the DANAERO project [**1**], so data has been also been extracted from there for verification. For the calibration procedure, the following steps are performed:

- Conversion of the raw data [in volts] into pressure data [PSI] using (**Eq 1**). The constants used are shown in **Table 5**.

$$P[PSI] = c_1 P_{raw}[V] + c_0 \quad \textbf{(Eq. 1)}$$

Table 5 - Calibration constants for raw Pitot tube pressures.

Sensor	Constant	C_1 (gain)	C_0 (offset)
C07-70-1	P_{16}	0.5	-0.0200
C07-70-1	P_{45}	0.5	0.0230
C07-70-2	P_{16}	0.5	-0.0002
C07-70-2	P_{45}	0.5	0.0257

The gain and offset coefficients depend on the pressure transducers and are temperature sensitive. Due to the lack of information of the serial number of the used transducers, a gain of 0.5 is used in all channels (0.4929-0.5096 for documented sensors). The offset values have been calculated from standstill measurements on the rotating rig, at low wind speeds.

- The pressures are converted from PSI to Torr since the coefficients are based on Torr.
- The pitch coefficient (C_α) is calculated from the differential pressures, according to **Eq. 2**.

$$C_a = \frac{P_{45}}{P_{16}} \quad \textbf{(Eq. 2)}$$

- The pitch angle α is calculated using a 4th order polynomial (**Eq. 3**), where the coefficients for the lowest Mach nr available (M=0.088) are shown in **Table 6**.

$$\alpha_{pitot} = a_0 + a_1 \cdot C_a + a_2 \cdot {C_a}^2 + a_3 \cdot {C_a}^4 + a_4 \cdot {C_a}^5 \quad \textbf{(Eq. 3)}$$

The angle of attack can be calculated, by offsetting the Pitot tube angle in relation to the chord, using **Eq. 4**. The Pitot angles in relation to the chord are 8.91 deg (outboard tube – 'tip') and 10.75 deg (inboard tube – 'rod'). This is extracted from image processing.

$$\alpha = a_{pitot} + \theta_{pitot} \quad \textbf{(Eq. 4)}$$

Table 6 -Coefficients for pitch angle calibration.

Constant	α_0	α_1	α_2	α_3	α_4
C07-70-1	1.36	15	0.162	-0.295	-0.12
C07-70-2	1.24	14.7	-0.0978	0.1249	0.314

- The dynamic pressure coefficient C_q is calculated using a 6th order polynomial (**Eq. 5**), where the coefficients for the lowest Mach nr available (M=0.088) are shown in **Table 7**.

$$C_q = a_{0,q} + a_{1,q} \cdot C_a + a_{2,q} \cdot {C_a}^2 + a_{3,q} \cdot {C_a}^3 + a_{4,q} \cdot {C_a}^4 + a_{5,q} \cdot {C_a}^5 + a_{6,q} \cdot {C_a}^6 \quad \textbf{(Eq. 5)}$$

Table 7 - Coefficients for dynamic pressure calibration.

Constant	$\alpha_{0,q}$	$\alpha_{1,q}$	$\alpha_{2,q}$	$\alpha_{3,q}$	$\alpha_{4,q}$	$\alpha_{5,q}$	$\alpha_{6,q}$
C07-70-1	0.999	0.0163	-0.0195	-0.0136	-0.0452	0.00320	0.011
C07-70-2	1	0.013	-0.0195	-0.00280	-0.0371	0.00650	0.0127

Since only the P_{45} signal is available in the current setup, there coefficients are based on the assumption that the 'pitch' angle α is always larger than the 'sideslip' angle β.

- The dynamic pressure is calculated based on **Eq. 6**.

$$Q = \frac{P_{16}}{C_q} \quad \textbf{(Eq. 6)}$$

- The velocity is calculated based on **Eq. 7**, where ρ is the air density at the specific measurement and 133.3223 is the conversion from [Torr] to [Pa].

$$V = \sqrt{\frac{2 \cdot Q \cdot 133.3226}{\rho}} \quad \textbf{(Eq. 7)}$$

Pressure taps details and calibration

The test section surface pressure distribution measurement is achieved utilizing a Scanivalve system, with 2.5psi range transducers.

The fully instrumented blade test section comprises 59 pressure taps in chordwise direction and 16 pressure taps in the chordwise direction.

The details on the chordwise pressure tap locations are shown in **Table 8**, and for the chordwise tap locations in **Table 9**.

Table 8 - Numbering and position of spanwise pressure taps.

Pressure hole nr	Profile hole nr	x [m]	y [m]	s [cm]	z [cm]	Pressure range [psi]	Side
1	61	0.9170	-0.0125	16.3626	-1.83	2.5	suction

2	60	0.8385	-0.0240	23.34251	-0.97	2.5	suction
3	59	0.7693	-0.0333	30.2621	0.00	2.5	suction
4	58	0.7006	-0.0419	37.10803	-5.33	2.5	suction
5	57	0.6326	-0.0498	43.89509	-4.13	2.5	suction
6	56	0.5651	-0.0569	49.78483	-2.88	2.5	suction
7	55	0.5065	-0.0621	55.61641	-1.43	2.5	suction
8	54	0.4483	-0.0663	60.59163	0.00	2.5	suction
9	53	0.3986	-0.0692	65.52852	-5.22	2.5	suction
10	52	0.3493	-0.0710	70.41226	-3.44	2.5	suction
11	51	0.3005	-0.0717	74.47914	-1.80	2.5	suction
12	50	0.2598	-0.0713	78.51511	0.00	2.5	suction
13	49	0.2195	-0.0698	81.7233	-5.41	2.5	suction
14	48	0.1875	-0.0675	84.60477	-3.87	2.5	suction
15	47	0.1588	-0.0646	87.17384	-2.39	2.5	suction
16	46	0.1333	-0.0615	89.40558	-1.10	2.5	suction
17	45	0.1113	-0.0577	91.31375	0.00	2.5	suction
18	44	0.0926	-0.0538	93.08026	-5.63	2.5	suction
19	43	0.0755	-0.0496	94.68063	-4.71	2.5	suction
20	42	0.0601	-0.0450	96.13589	-3.87	2.5	suction
21	41	0.0465	-0.0400	97.41353	-3.13	2.5	suction
22	40	0.0348	-0.0348	98.56549	-2.47	2.5	suction
23	39	0.0246	-0.0294	99.46688	-1.95	2.5	suction
24	38	0.0171	-0.0244	100.2479	-1.49	2.5	suction
25	37	0.0111	-0.0194	100.8475	-1.15	2.5	suction
26	36	0.0070	-0.0150	101.3856	-0.84	2.5	suction
27	35	0.0039	-0.0106	101.8522	-0.57	2.5	suction
28	34	0.0018	-0.0065	102.2267	-0.35	2.5	suction
29	33	0.0006	-0.0029	102.5238	-0.18	2.5	suction
30	32	0.0000	0.0000		0	2.5	LE
31	31	0.0006	0.0029	102.5238	0.18	2.5	pressure
32	30	0.0018	0.0065	102.2267	0.35	2.5	pressure
33	29	0.0039	0.0106	101.8522	0.57	2.5	pressure
34	28	0.0070	0.0150	101.3856	0.84	2.5	pressure
35	27	0.0111	0.0194	100.8475	1.15	2.5	pressure
36	26	0.0171	0.0244	100.2479	1.49	2.5	pressure
37	25	0.0246	0.0294	99.46688	1.95	2.5	pressure
38	24	0.0348	0.0348	98.56549	2.47	2.5	pressure
39	23	0.0465	0.0400	97.41353	3.13	2.5	pressure
40	22	0.0601	0.0450	96.13589	3.87	2.5	pressure
41	21	0.0755	0.0496	94.68063	4.71	2.5	pressure
42	20	0.0926	0.0538	93.08026	5.63	2.5	pressure
43	19	0.1113	0.0577	91.31375	0.00	2.5	pressure

44	18	0.1333	0.0615	89.40558	1.10	2.5	pressure
45	17	0.1588	0.0646	87.17384	2.39	2.5	pressure
46	16	0.1875	0.0675	84.60477	3.87	2.5	pressure
47	15	0.2195	0.0698	81.7233	5.41	2.5	pressure
48	14	0.2598	0.0713	78.51511	0.00	2.5	pressure
49	13	0.3005	0.0717	74.47914	1.80	2.5	pressure
50	12	0.3493	0.0710	70.41226	3.44	2.5	pressure
51	11	0.3986	0.0692	65.52852	5.22	2.5	pressure
52	10	0.4483	0.0663	60.59163	0.00	2.5	pressure
53	9	0.5065	0.0621	55.61641	1.43	2.5	pressure
54	8	0.5651	0.0569	49.78483	2.88	2.5	pressure
55	7	0.6326	0.0498	43.89509	4.13	2.5	pressure
56	6	0.7006	0.0419	37.10803	5.33	2.5	pressure
57	5	0.7693	0.0333	30.2621	0.00	2.5	pressure
58	4	0.8385	0.0240	23.34251	0.97	2.5	pressure
59	3	0.9170	0.0125	16.3626	1.83	2.5	pressure

Table 9 - Numbering and position of chordwise pressure taps.

Pressure hole nr	Profile hole nr	x [m]	y [m]	s [cm]	z [cm]	Pressure range [psi]	Side
1	1	0.25	0.07	78	-103.125	2.5	suction
2	2	0.25	0.07	78	-89.375	2.5	suction
3	3	0.25	0.07	78	-75.625	2.5	suction
4	4	0.25	0.07	78	-61.875	2.5	suction
5	5	0.25	0.07	78	-48.125	2.5	suction
6	6	0.25	0.07	78	-34.375	2.5	suction
7	7	0.25	0.07	78	-20.625	2.5	suction
8	8	0.25	0.07	78	-6.875	2.5	suction
9	9	0.25	0.07	78	6.875	2.5	suction
10	10	0.25	0.07	78	20.625	2.5	suction
11	11	0.25	0.07	78	34.375	2.5	suction
12	12	0.25	0.07	78	48.125	2.5	suction
13	13	0.25	0.07	78	61.875	2.5	suction
14	14	0.25	0.07	78	75.625	2.5	suction
15	15	0.25	0.07	78	89.375	2.5	suction
16	16	0.25	0.07	78	103.125	2.5	suction

Strain gauges details and calibration

Strain gauges are located close to the blade section (0.5m from connection) and close to the root of the boom (0.67m from connection).

A pull test is performed on 04-09-2014 in order to calibrate the strain gauge sensors. The blade is pulled towards the tower in the flapwise test (**Figure 54** - left) and towards the ground in the edgewise test (**Figure 54** - right). A force gauge is used in order to record the pull force signal.

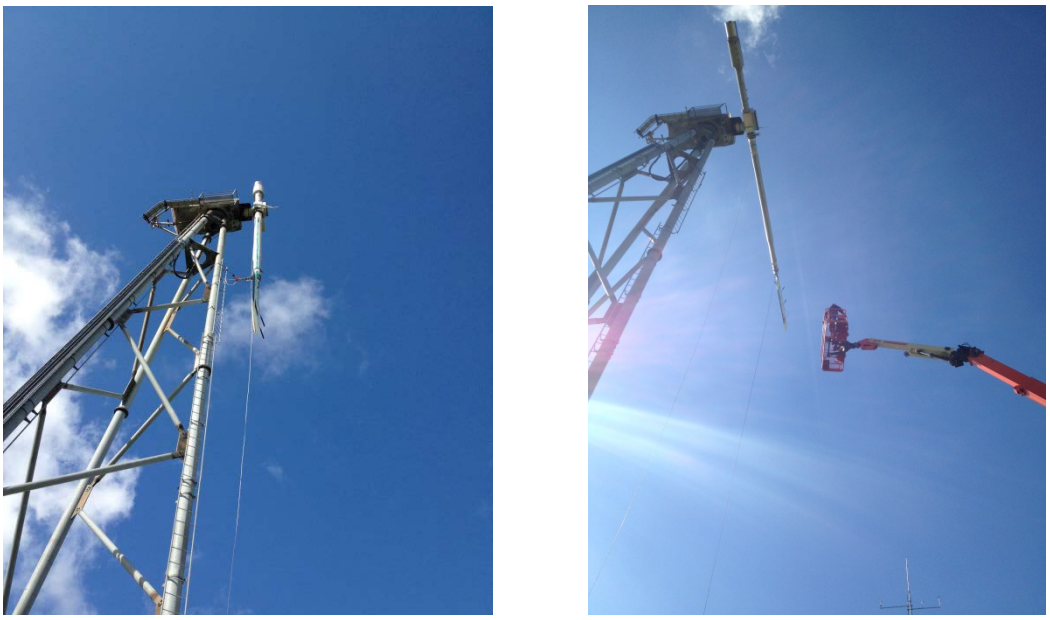

Figure 54 – Pull tests (left: flapwise, right: edgewise).

The flapwise pull test time series showing the applied pull force and the measured root strain signal is shown in the figure on the left. The pull force versus the measured strain is shown in the figure on the right, where a linear function is fitted.

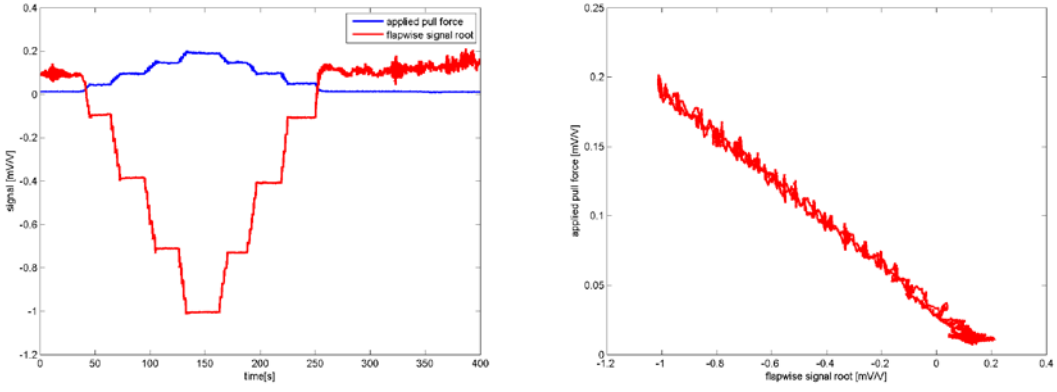

Figure 55 – Boom root flapwise pull test signals (left: time series, right: linear regression).

The results for the flapwise pull test are also shown in **Figure 56** for the strains gauge close to the blade section.

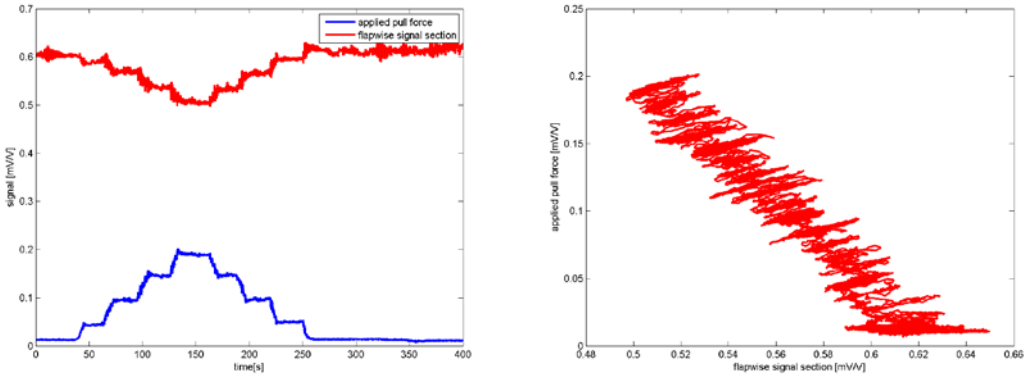

Figure 56 – Blade section flapwise pull test signals (left: time series, right: linear regression).

The edgewise pull test time series showing the applied pull force and the measured strain signal is shown in **Figure 57** on the left. The pull force versus the measured strain is shown in **Figure 57** on the right, where a linear function is fitted. The strain sensor signal for initial (assumed zero) force pull has been subtracted from the total signal in order to account for the gravity contribution to the edgewise strains.

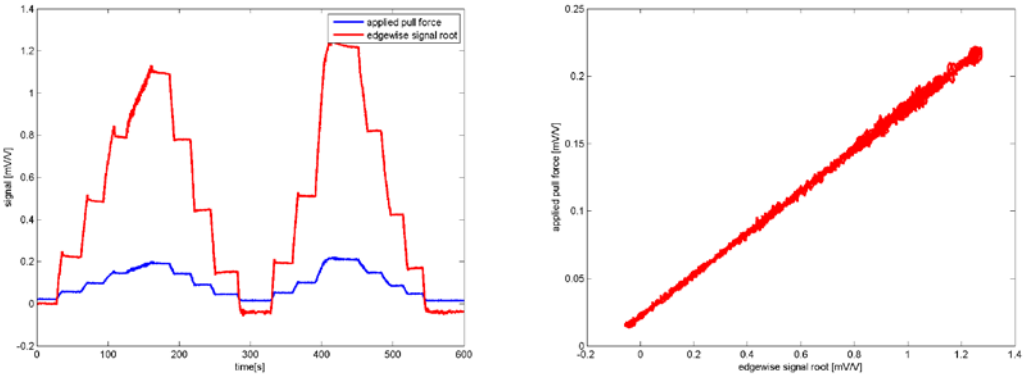

Figure 57 – Boom root edgewise pull test signals (left: time series, right: linear regression).

In order to convert the signals to bending moment values, the following relations are used (**Eq. 8-11**):

$$M_{flap,root}[Nm] = \alpha_1 \cdot \beta_1 \cdot SG_{flap}\left[\frac{mV}{V}\right] + \gamma_1 \quad \textbf{(Eq. 8)}$$

$$M_{edge,root}[Nm] = \alpha_2 \cdot \beta_2 \cdot SG_{edge}\left[\frac{mV}{V}\right] + \gamma_2 \quad \textbf{(Eq. 9)}$$

$$M_{flap,section}[Nm] = \alpha_3 \cdot \beta_3 \cdot SG_{flap}\left[\frac{mV}{V}\right] + \gamma_3 \quad \textbf{(Eq. 10)}$$

$$M_{edge,section}[Nm] = \alpha_4 \cdot \beta_4 \cdot SG_{edge}\left[\frac{mV}{V}\right] + \gamma_4 \quad \textbf{(Eq. 11)}$$

The *α*, *β*, *γ* gains are extracted from the linear regression and are shown in **Table 10**. This was not possible for the section edgewise signal since due to a false connection, it was logging the torsional sensor data.

Table 10 - Calibration parameters for strain gauge sensors.

	1	**2**	**3**	**4**
α	-0.1592	0.1549	-1.6680	0
β	148590	151033	9409	11853
γ	0.0313	0.0219	1.0360	0

The *β* gains are calculated as follows (**Eq 12**):

$$\beta_{1,2,3,4} = g_t \cdot g \cdot \cos\theta_{tilt} \cdot r_{arm} \quad \textbf{(Eq. 12)}$$

where g_t=2500 [kgV/mV] is the gain to calibrate the pull force transducer from [mV] to [kg], *g*=9.813[m/s^2] is the gravitational acceleration, $\theta_{tilt}=5^o$ is the rotor tilt angle and r_{arm} is the moment arm from the pull force application point to the strain gauge position (**Table 11**).

Table 11 – Force-sensor distances for pull tests.

r_{arm}	**r,f**	**r,e**	**b,f**	**b,e**
Value	6.08	6.18	0.385	0.485

Pitch angle calibration

A test is performed on 11-09-2014 in order to calibrate the pitch sensor. A range of pitch command signal inputs is given and the pitch position signal is measured. At the same time, photos of the blade section at a downward position are taken from the ground in order to identify the actual pitch angle. The pitch angle is defined by the difference in orientation of the computer box front surface on the hub (which is assumed to be parallel to the rotor plane) and the chordline of the aerofoil section. Reference photos for a range of 0V to 6V in the command input signal are shown in **Figure 58**.

Figure 58 – Images for pitch calibration (pitch command signal 0-6V).

For a range of pitch input cases 0V-6V, 3 different photos are used (6 photos for the 0V input case). The images are processed by manually identifying the edges of the reference lines, then

calculating the distances in pixels and calculating the angle differences with respect to the horizontal dimension of the image frame. The difference in those angles between the two lines is then treated as the geometric pitch angle. The average of the resulting pitch angles value from all images is used per input case and the average max/min error is identified (**Table 12**). A linear function is then fitted into the average data.

Table 12 –Pitch calibration results.

Pitch command [V]	Pitch position [V]	Pitch angle [V]	Error [±deg]
0	1.073	1.07	0.10
2	1.360	6.07	0.27
4	1.678	15.00	0.15
6	1.991	24.51	0.07

In order to convert the pitch position signals to geometric pitch angle values, the following relation is used:

$$Pitch\_angle[deg] = \alpha \cdot Pitch\_pos[V] + \beta \quad \textbf{(Eq. 13)}$$

Similarly, for the pitch command signal, the following relation is used:

$$Pitch\_angle[deg] = \gamma \cdot Pitch\_com[V] + \delta \quad \textbf{(Eq. 14)}$$

The α, β, γ, δ gains are given in **Table 13**.

Table 13 – Pitch calibration parameters.

Factor	α	β	γ	δ
Value	25.24	-26.67	3.86	0.23

The pitch angle calibration is used as an indication of the fixed pitch setpoint, since no dynamic pitch test are possible with the current setup. The Pitot tube signals are used in order to acquire the resulting inflow angles.

7. Aeroelastic model and simulations of the test rig

The HAWC [**1**] aeroelastic model utilized to simulate the rotating test rig is described in this section, covering details about the input data and modelling options, and computed results of modal analysis, aeroelastic loads, and aerodynamic performance are presented. The described model is based on a series of previous HAWC2 models of the Tellus turbine and the rotating rig, and has been was updated based on the available details of the new designed and manufactured component.

Assembly modelling

The rotating rig has been represented in HAWC2 as an assembly of eight bodies consisting of Timoshenko beam elements (**Figure 59**).

The body constraints, following the order of the multi-body chain, are:

- The tower is rigidly connected to the ground.
- The yaw ring can rotate with an action command control input relative to the tower end.
- The shaft can rotate with a specified angular velocity relative to the yaw ring end.
- The hub is rigidly connected to the shaft end.
- The extension to the boom side is rigidly connected to the hub end.
- The boom can rotate with an action command control input relative to the extension end.
- The extension to the counterweight side is rigidly connected to the hub end.
- The counter-weight is rigidly connected to the extension.

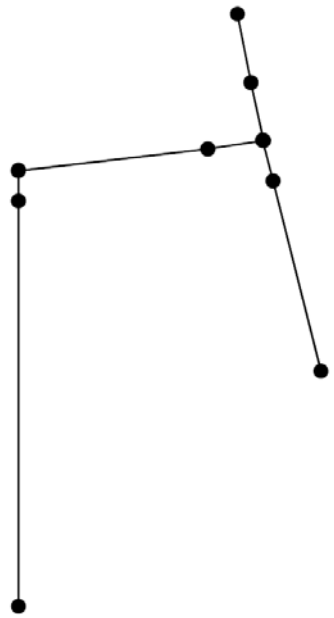

Figure 59 - Structural assembly in HAWC2

The HAWC2 geometry representation in HAWC2 is shown in **Figure 60**.

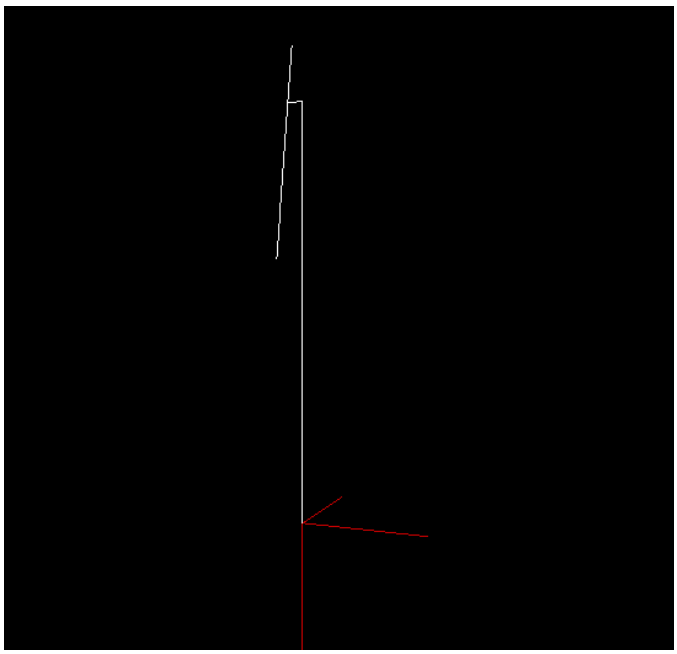

Figure 60 - HAWC2 structural assembly representation

Structural input data

Each body is modelled by specifying structural input data at a sectional level. A summary of the body length and mass properties is shown in **Table 14**. For the boom and the counterweight, the length of the different parts modelled is also included.

Table 14 - Length and mass of bodies and segments.

body	section	Length [m]	Mass [kg]
tower	all	30.000	7411.910
yaw ring	all	0.100	4309.000
shaft	all	0.600	270.600
hub	all	0.700	549.780
extension to boom	all	0.372	63.884
boom	all	10.939	478.244
boom	base	0.335	46.993
boom	beam 1	5.149	143.417
boom	connection 1	0.300	7.032
boom	beam 2	1.500	31.820
boom	connection 2	0.475	28.989
boom	inner end cap	0.500	26.750
boom	wing	2.400	199.920
boom	outer end cap	0.500	26.750
extension to counter-weight	all	0.642	141.603
counter-weight	all	3.448	874.290
counter-weight	beam 1	1.998	165.3760
counter-weight	beam 2	1.000	170.5360
counter-weight	weight	0.450	538.3780

For the tower, yaw ring, and shaft, existing data is used, which is based on the modelling of the 100kW Tellus turbine [**3**].

For the rest (new designed components), the structural input data is calculated utilizing the 3D CAD representation of the components, which has been used for manufacturing. The structural data needed for the calculation of the required data for HAWC2 is extracted from the assemblies of the components in the CATIA software. This consists of the length (*dr*), mass (*m*), mass moment of inertia (I_{zz}), area moments of inertia (I_x, I_y, I_z) and cross-sectional area (*A*). The 3D properties referring to a solid volume (*m*, I_{zz}) are calculated from the assembly segments at the corresponding span-wise distance of the section of interest. The cross sectional properties (I_x, I_y, I_z, *A*) are calculated on a reference cross section of the 3D segment, providing average properties. For long segments (e.g. beam parts of the boom) segments of 0.5m span-wise length are used, so 3D properties are then calculated based on those. The mass per unit length and the radii of inertia are calculated as shown in **Eq. 15** and **Eq. 16.** Most of the segments are symmetrical around their span-wise axis, so in this case, ri_x and ri_y are equal, satisfying **Eq. 17**, and the centres of gravity, elasticity, and shear lie on the reference axis.

$$dm = \frac{m}{dr} \quad \textbf{(Eq. 15)}$$

$$r = \sqrt{\frac{I_{zz}}{m}} \quad \textbf{(Eq. 16)}$$

$$r^2 = r_{ix}^2 + r_{iy}^2 \quad \textbf{(Eq. 17)}$$

For the boom, the segments are defined as shown in Table 1. The 3D model of the boom assembly is shown in **Figure 61 (**note: the wing end caps are not shown in this assembly**).** The structural data from the wing section is extracted from the corresponding 3D model of its assembly (reference to report or other section, or more info needed here!).

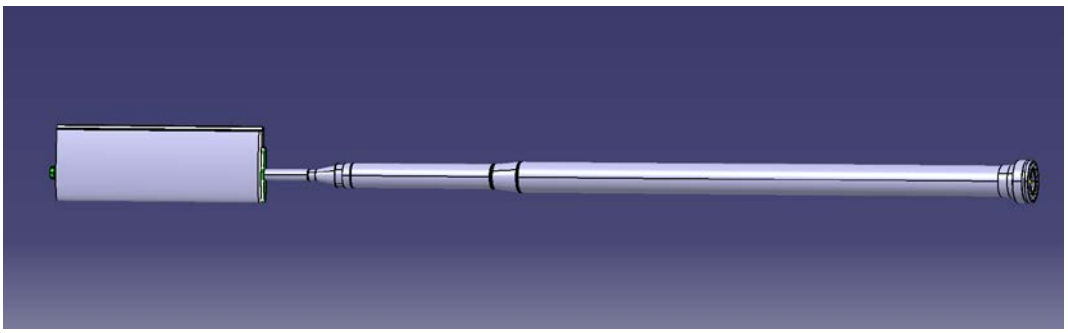

Figure 61 - 3D model of the boom assembly.

The calculated span-wise distribution of mass, radii of inertia, area moments of inertia and cross sectional area is shown in **Figure 62, Figure 63, Figure 64,** and **Figure 65** respectively. Material elastic moduli are defined for aluminium (*E*=72 GPa, *G*=25 GPa), for all segments except for the wing section.

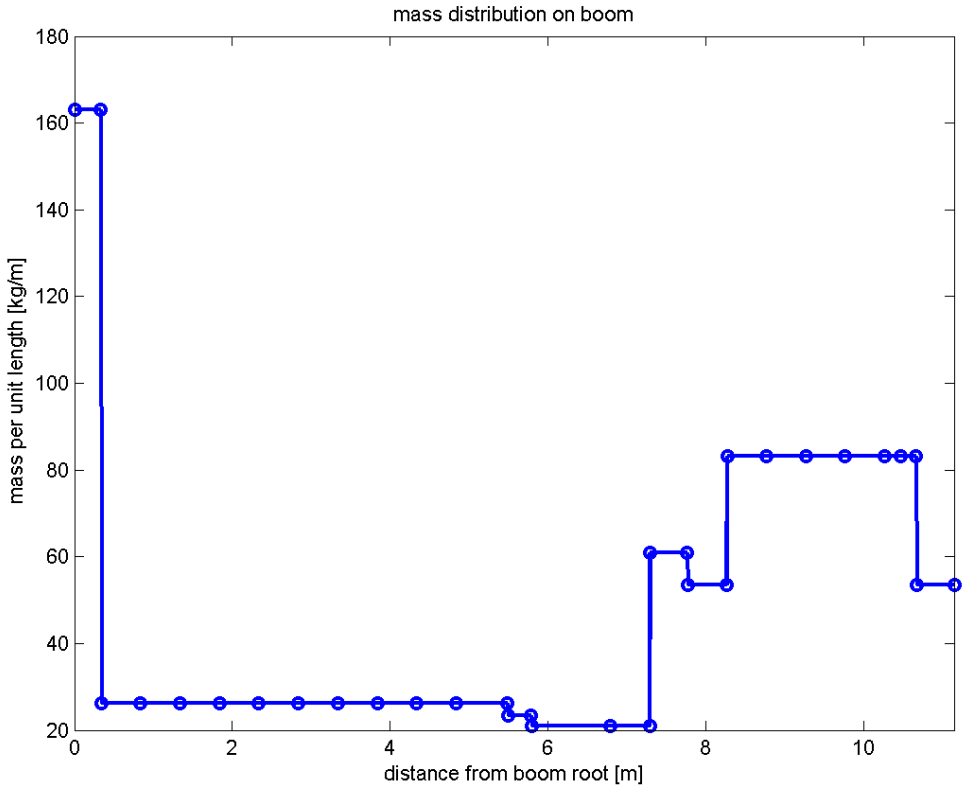

Figure 62 - Mass distribution on boom.

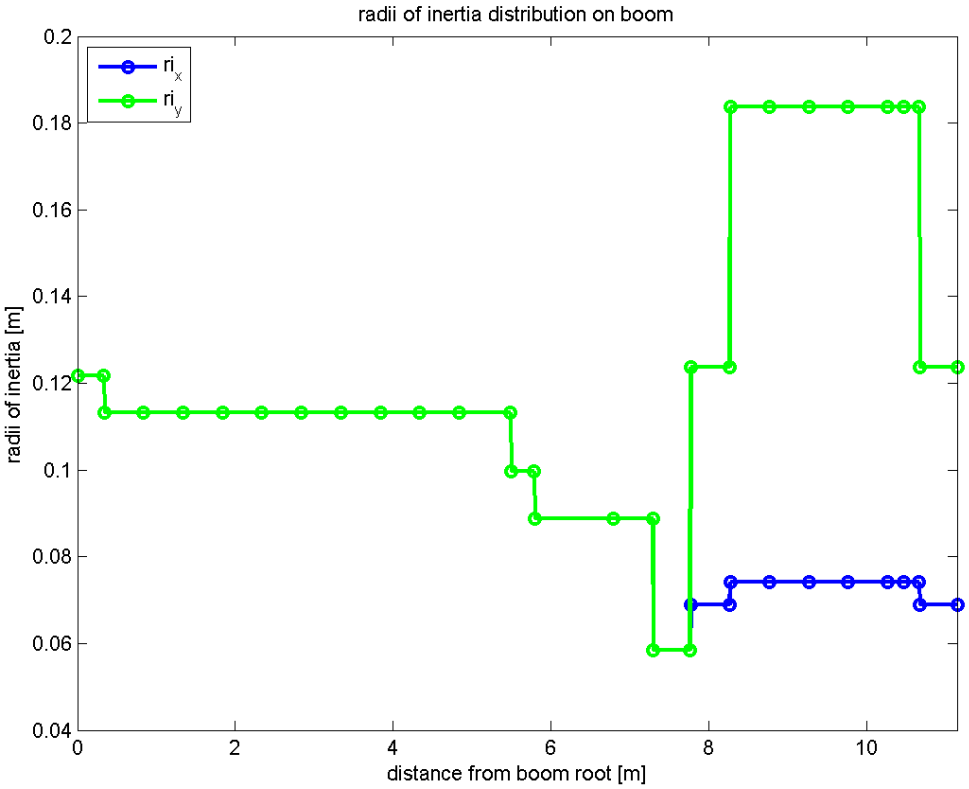

Figure 63 -Radii of inertia distribution on boom.

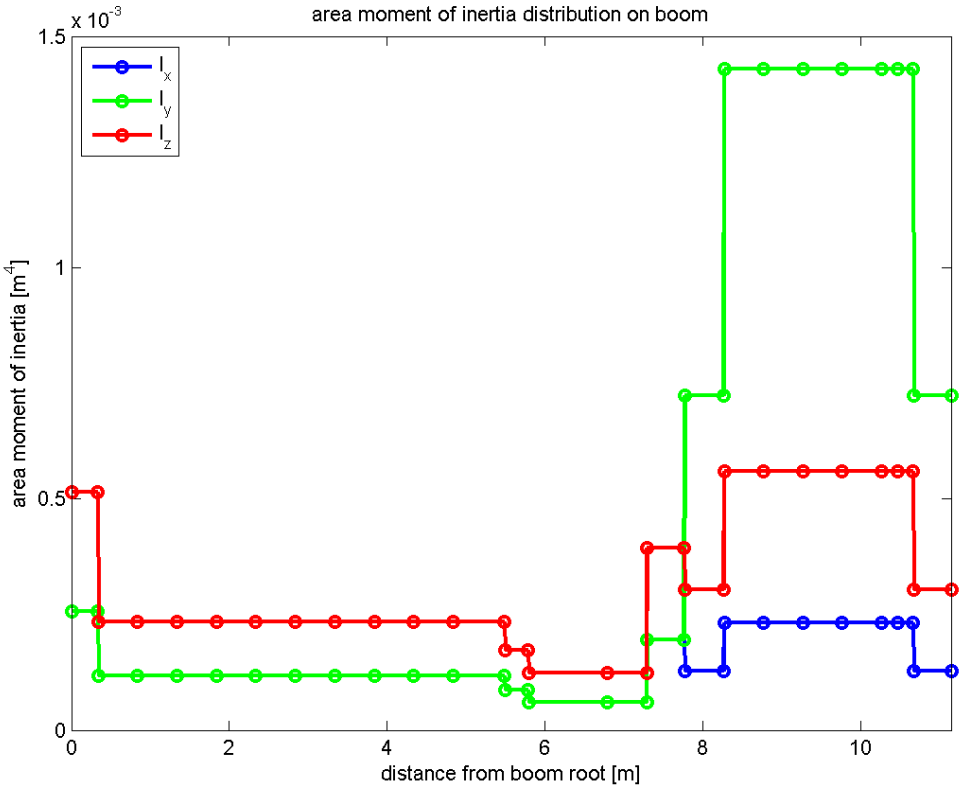

Figure 64 - Area moment of inertia distribution on boom.

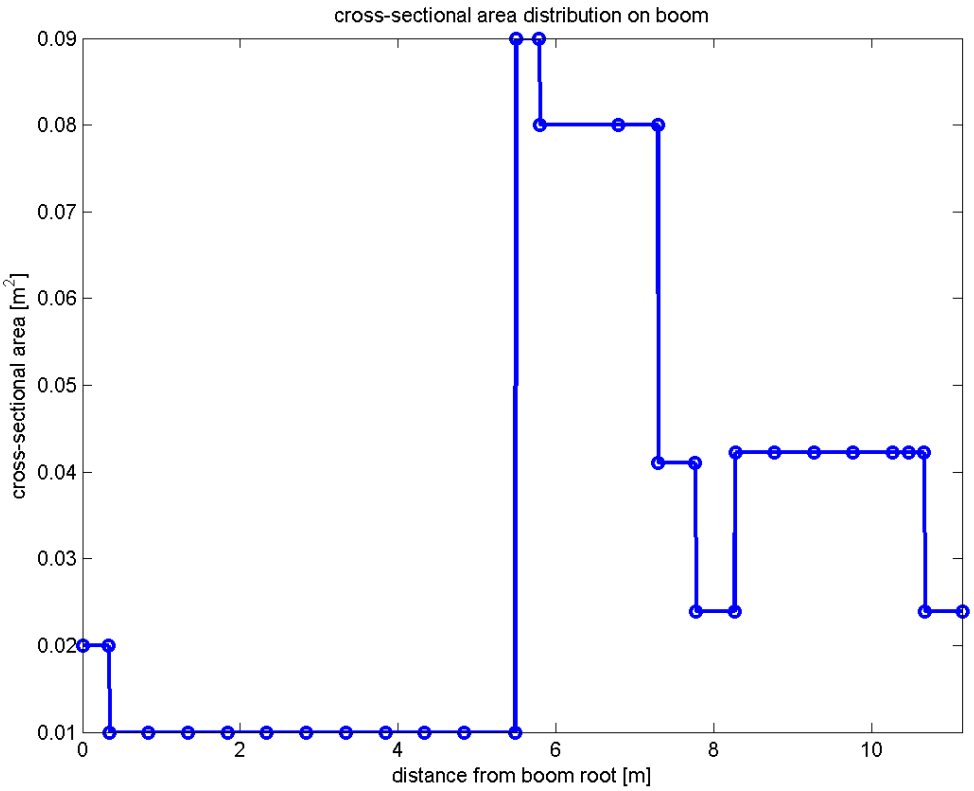

Figure 65 - Cross-sectional area distribution on boom.

For the counterweight, the segments are defined as shown in **Table 2**. The 3D model of the boom assembly is shown in **Figure 66.**

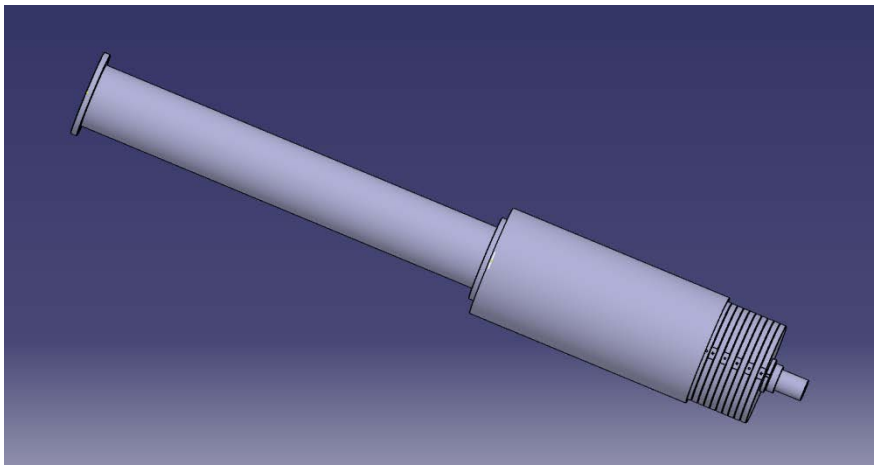

Figure 66 - 3D model of the counterweight assembly.

The calculated span-wise distribution of mass, radii of inertia, area moments of inertia and cross sectional area is shown in **Figure 67**, **Figure 68**, **Figure 69**, and **Figure 70** respectively. Material elastic moduli are defined for steel (*E*=210 GPa, *G*=60 GPa).

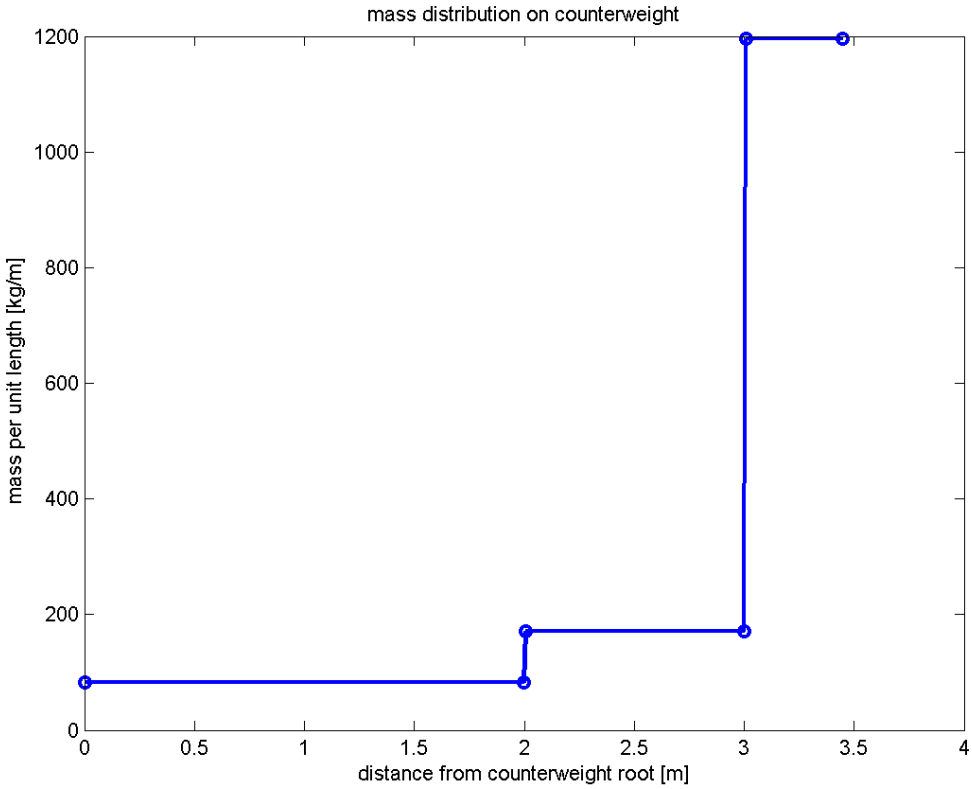

Figure 67 - Mass distribution on counterweight.

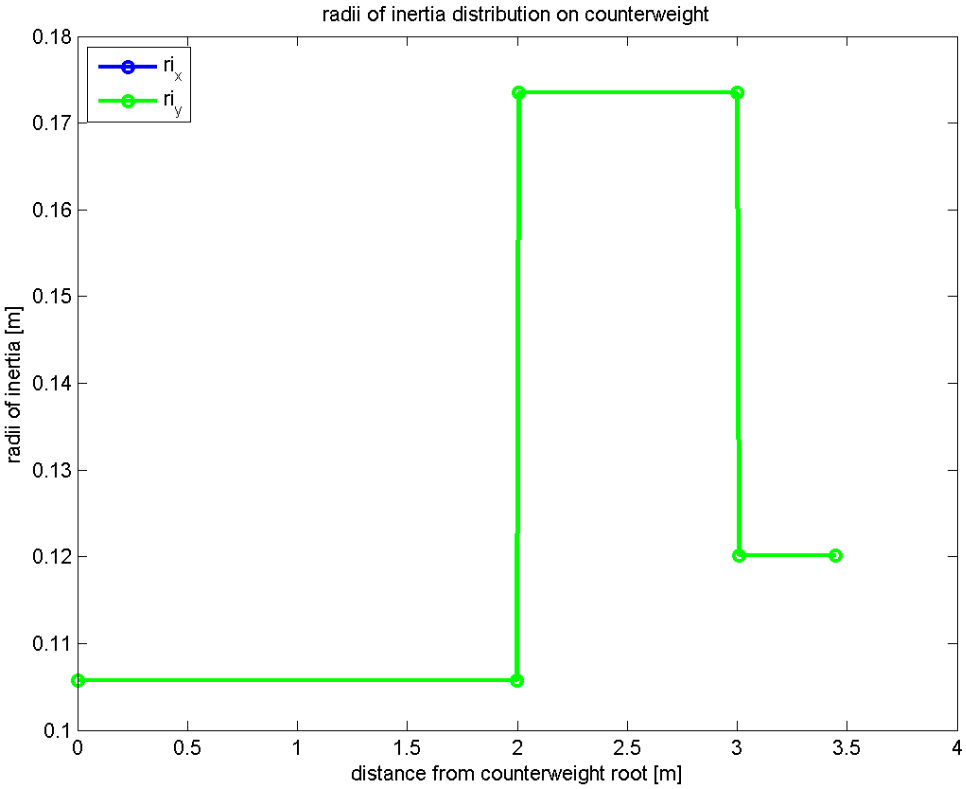

Figure 68 - Radii of inertia distribution on counterweight.

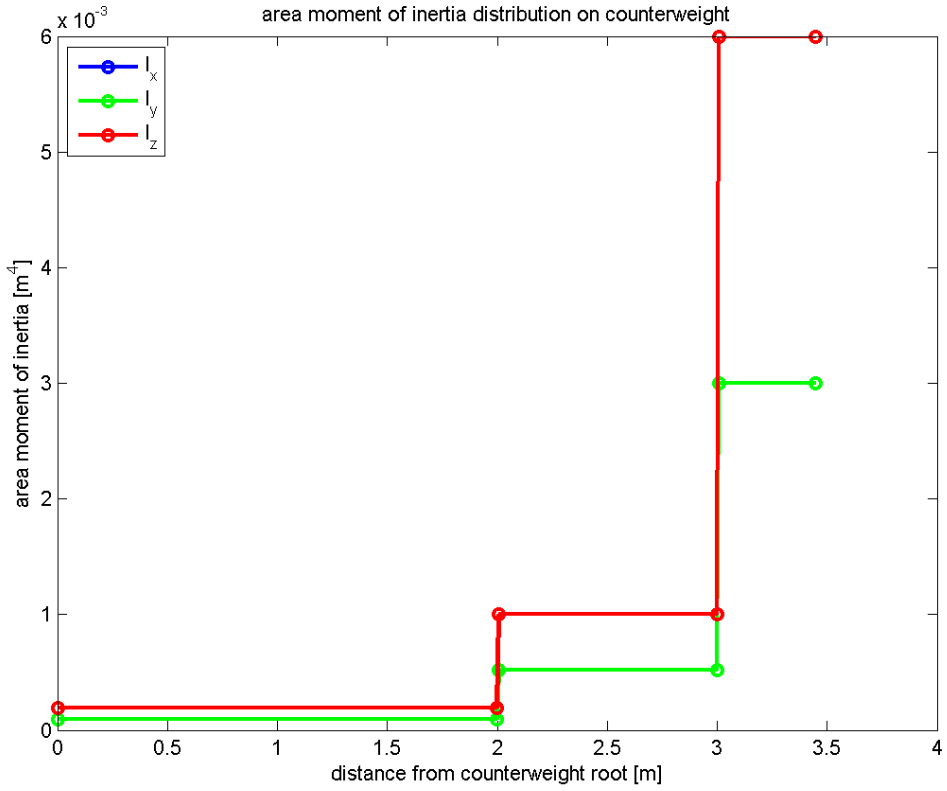

Figure 69 - Area moment of inertia distribution on counterweight.

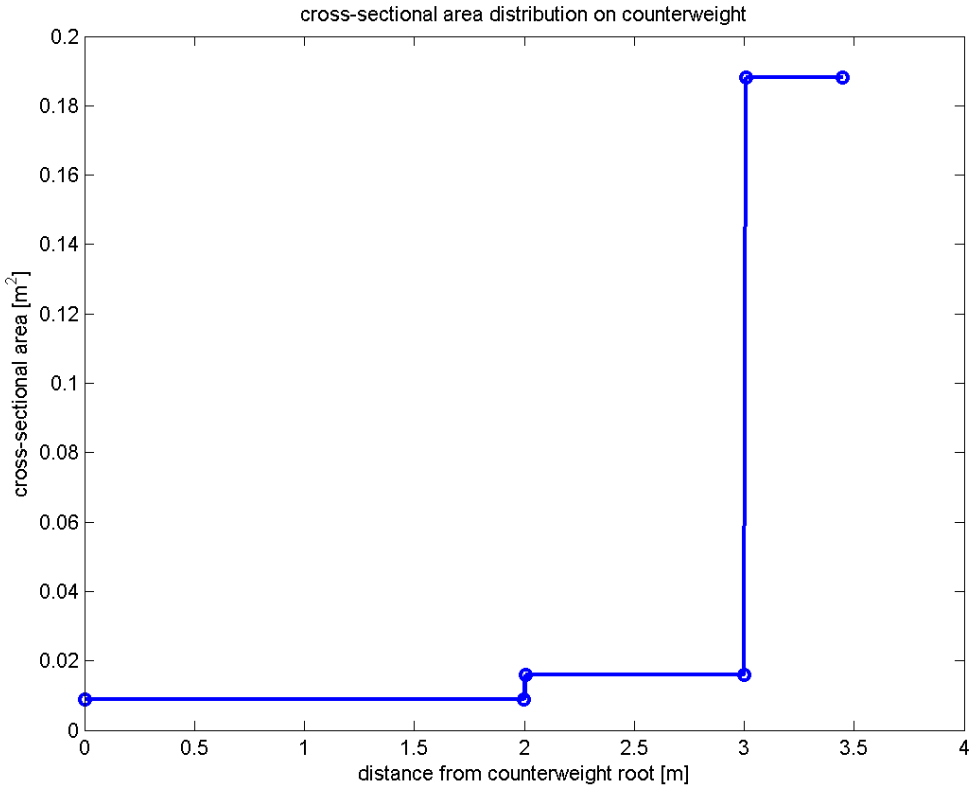

Figure 70 - Cross-sectional area distribution on counter-weight.

In order to extract structural data for the hub and the two extension bodies, certain assumptions are made. In **Figure 71**, the hub assembly is shown, with the main structural parts. The hub body is defined based on the solid part of the assembly connected to the low motor shaft, excluding the body of pitch shaft. The extension to the boom is defined based on the pitch shaft body. The extension to the counterweight is defined based on the rectangular frame body, since the counterweight root is supported on it and not directly on the hub.

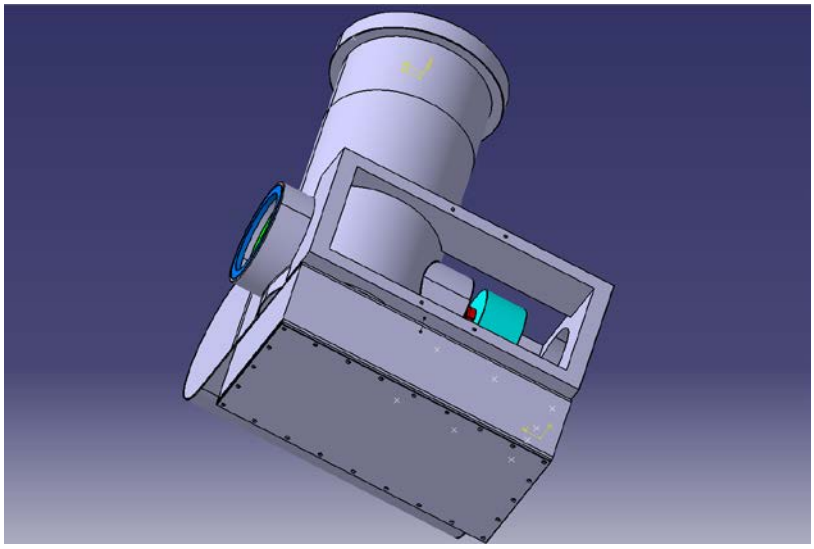

Figure 71 - 3D model of the hub assembly.

The calculated structural properties for the hub and extension bodies are shown in **Table 15**.

Table 15 - Structural properties for the hub and extension bodies.

body	Mass distribution [kg/m]	Radii of inertia [m]	Area moment of inertia [m^4]	Cross-sectional area
hub	785.400	0.128	0.001	0.058
extension to boom	171.731	0.063	0.001	0.015
extension to counter-weight	220.565	0.171	0.001	0.025

Aerodynamic input data

Aerodynamic input data is provided in HAWC2 only for the body representing the boom. The wing section with the end caps (**Figure 72**) is the main aerodynamic part utilizing data for the NACA0015 aerofoil, and the rest of the boom is defined as a drag-producing part. The chord and thickness distribution for the boom sections are shown in **Figure 73** and **Figure 74**.The constant chord part is 2.4m long and the two end caps are each 0.5m long.

Figure 72 - Wing section geometry.

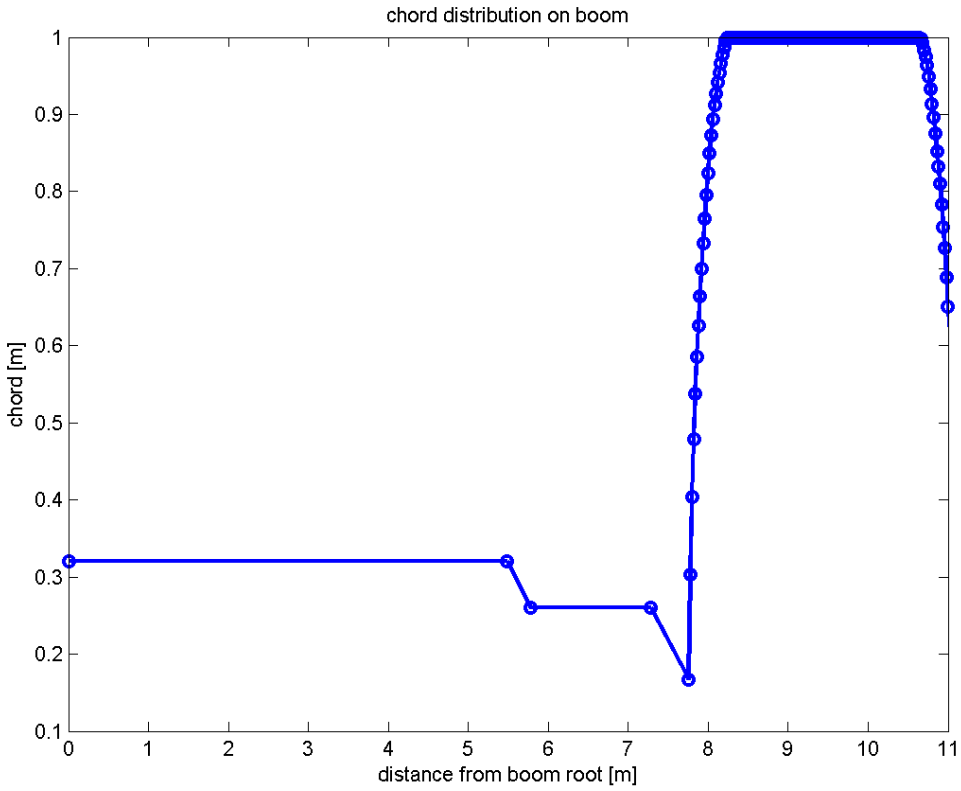

Figure 73 - Chord distribution on boom.

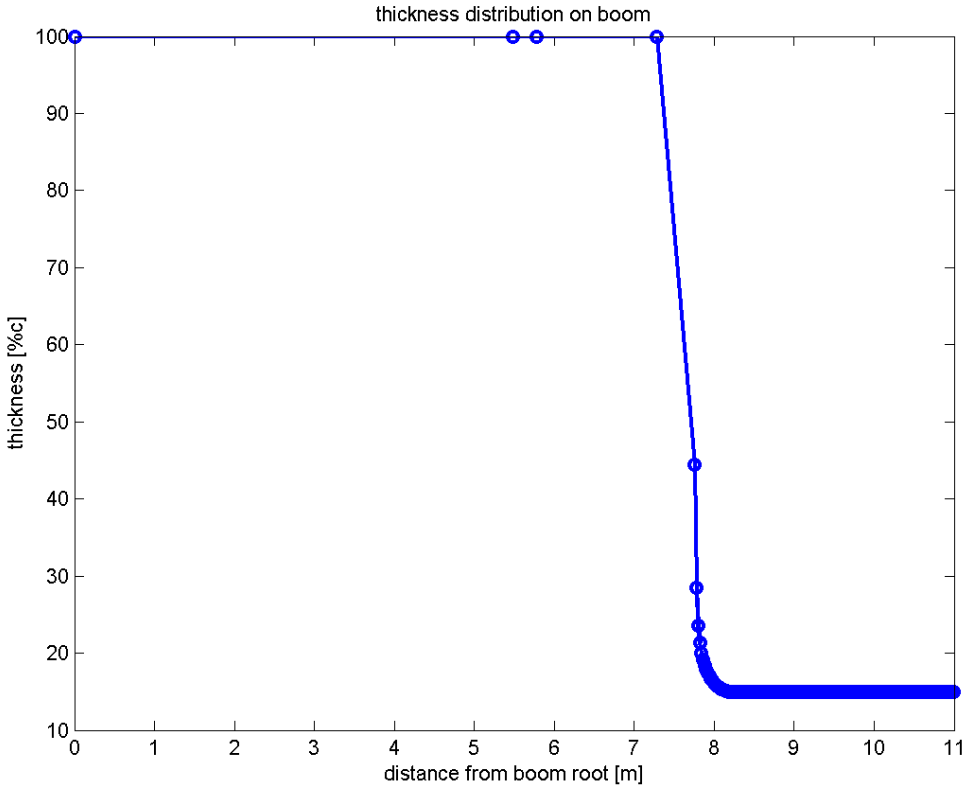

Figure 74 - Thickness distribution on boom.

Steady data for the NACA0015 aerofoil is produced using XFoil for Re=2.5·10^6 with free and turbulent boundary layer transition, where the data is blended with a 50% ratio. The C_l, C_d, and C_m polars for a normal angle of attack range are shown in **Figure 75**, **Figure 76**, and **Figure 77** respectively. The rest of the boom sections are modelled only specifying a C_d value of 0.8 for the whole angle of attack range. The hub extension sections (to the boom and to the counter-weight) are also modelled as drag elements using a C_d value of 0.8.

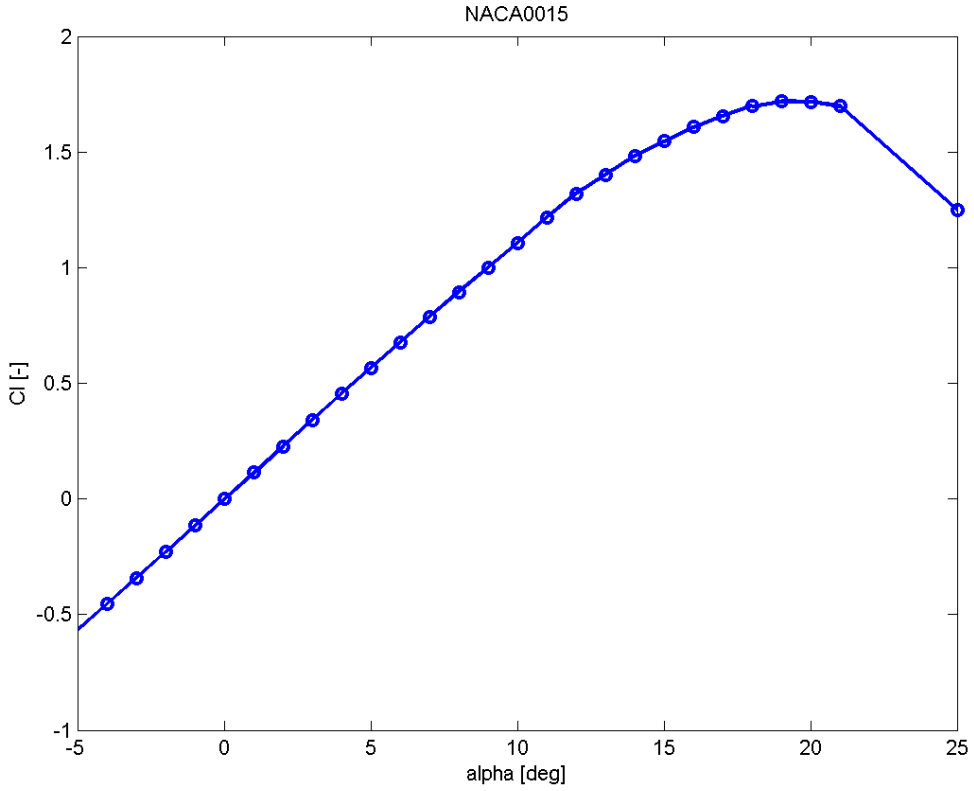

Figure 75 - Cl polar for NACA0015, XFoil Re=5mil.

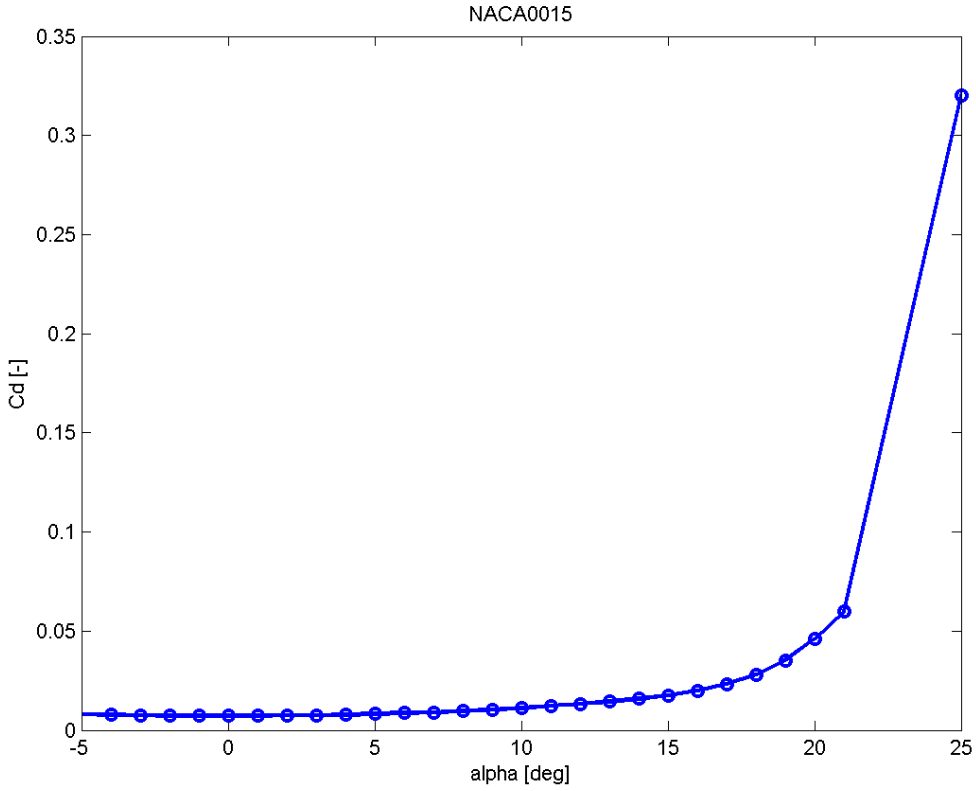

Figure 76 - C_d polar for NACA0015, XFoil Re=5mil.

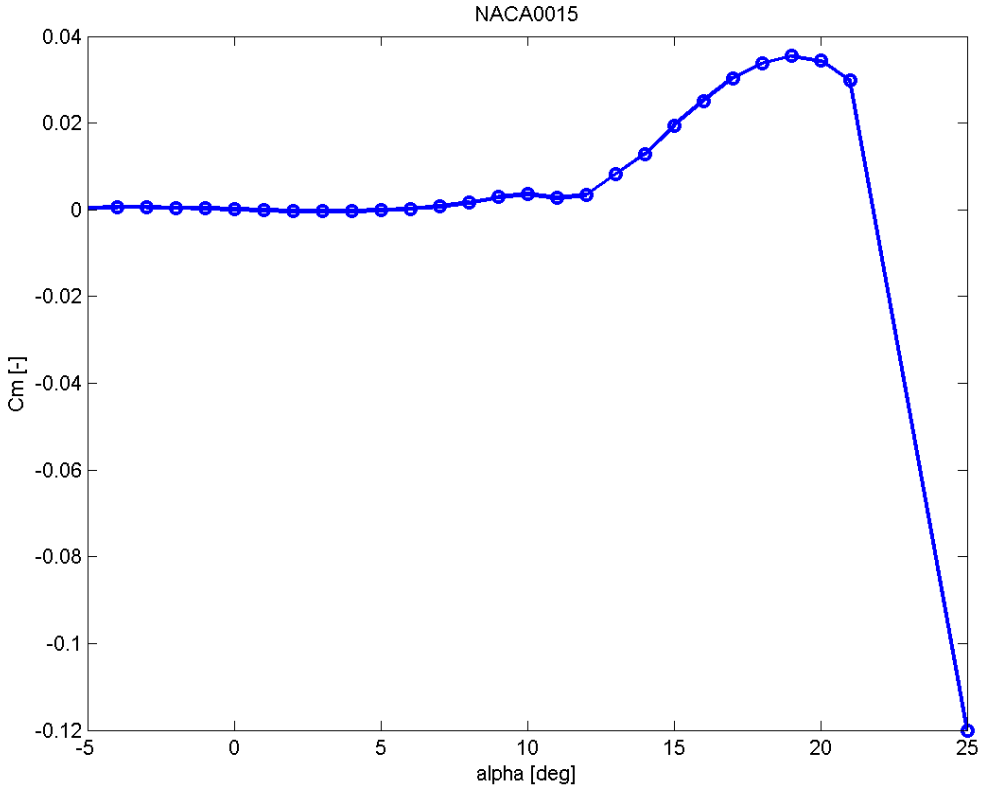

Figure 77 - C_m polar for NACA0015, XFoil Re=5mil.

Flaps input data

The ATEFlap dynamic stall model is utilized in order to model the unsteady aerodynamics of the 15%c flap section (covering the wing section, 8.2685m-10.4585m from the boom root) [**4**]. The additional input required for the modelling of the flap section aerodynamics is the steady variation of the aerodynamic coefficients at different angles of attack and flap deflections. These 'deltas' are produced using XFoil computations for $Re=2.5 \cdot 10^6$ with free and turbulent boundary layer transition, where the data is blended with a 50% ratio. The flap geometry utilized is based on earlier flap deflection shape measurements on CRTEF geometries (**Figure 78**).

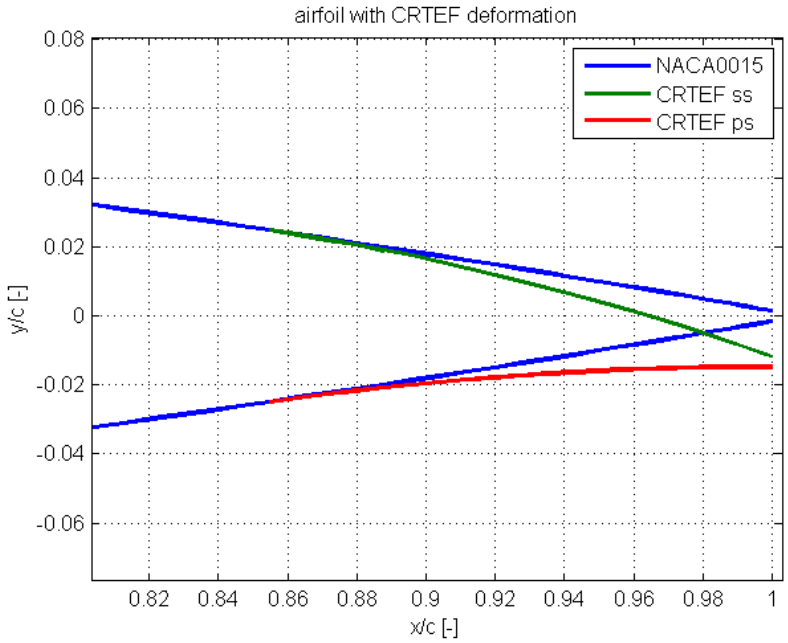

Figure 78 – +5 deg. deflection of a 15%c CRTEF on the NACA0015.

The calculated C_l, C_d, and C_m deltas for +/-5deg CRTEF deflections are shown in **Figure 79**.

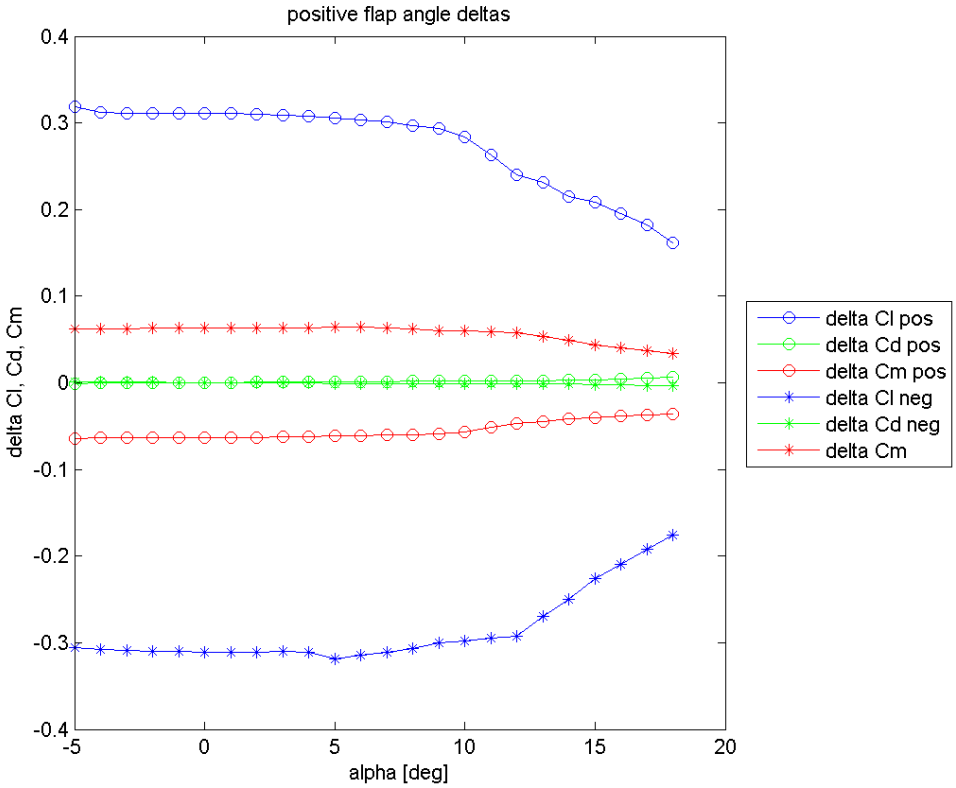

Figure 79 – Deltas Cl, Cd, Cm for +/-5deg CRTEF deflection.

The data is pre-processed together with the steady C_l, C_d, and C_m polar data for the aerofoil without flaps in order to generate the required input to the ATEFlap model. Standard indicial response parameters and time constants are used in the model.

Aerodynamics modelling options

In order to accurately model the rotor aerodynamics of the rotating rig, a near wake implementation in HAWC2 is utilized. The near wake model [**5**] accounts for the dynamic effects of the trailed vorticity close to the blade, and it is expected to give more realistic results compared to the normal dynamic inflow modelling of a rotor. No tip loss model is used together with the near wake model since the tip effects are already accounted for. The far wake contribution to induction is also discarded, since it will not be realistic on such a configuration. The ATEFlap dynamic stall model is utilized in combination with the existing rotor aerodynamics setup to account for the shed vorticity dynamics.

A comparison of the predicted axial induced velocities along the boom span utilizing different induction modelling options is shown in **Figure 80**. The near wake model is shown to predict high absolute values of induced velocities at the wing section region due to the large variations of the bound circulation. As expected, including tip losses in the normal induction model produces results closer to the near wake model.

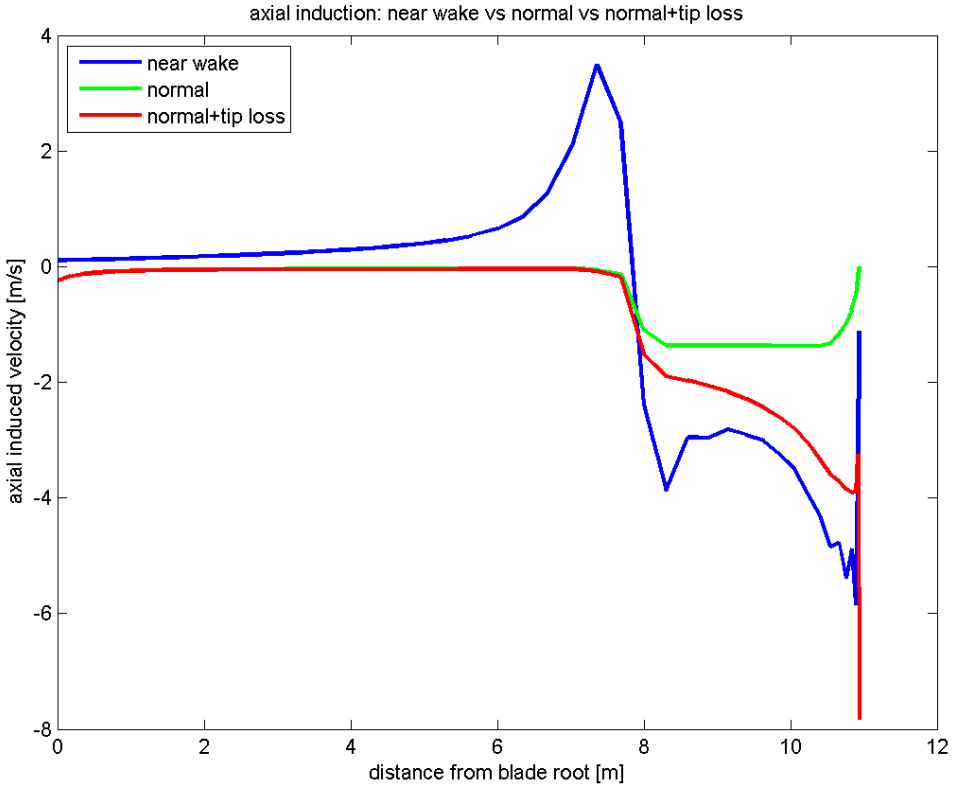

Figure 80 - Comparison of computed axial induced velocity along boom span (V=10m/s, ω=50rpm, pitch=0deg.).

A comparison of the predicted lift at every aerodynamic element utilizing the different induction modelling options is shown in **Figure 81**. It is seen that the normal induction modelling results in a considerable overprediction of aerodynamic loading at a sectional level.

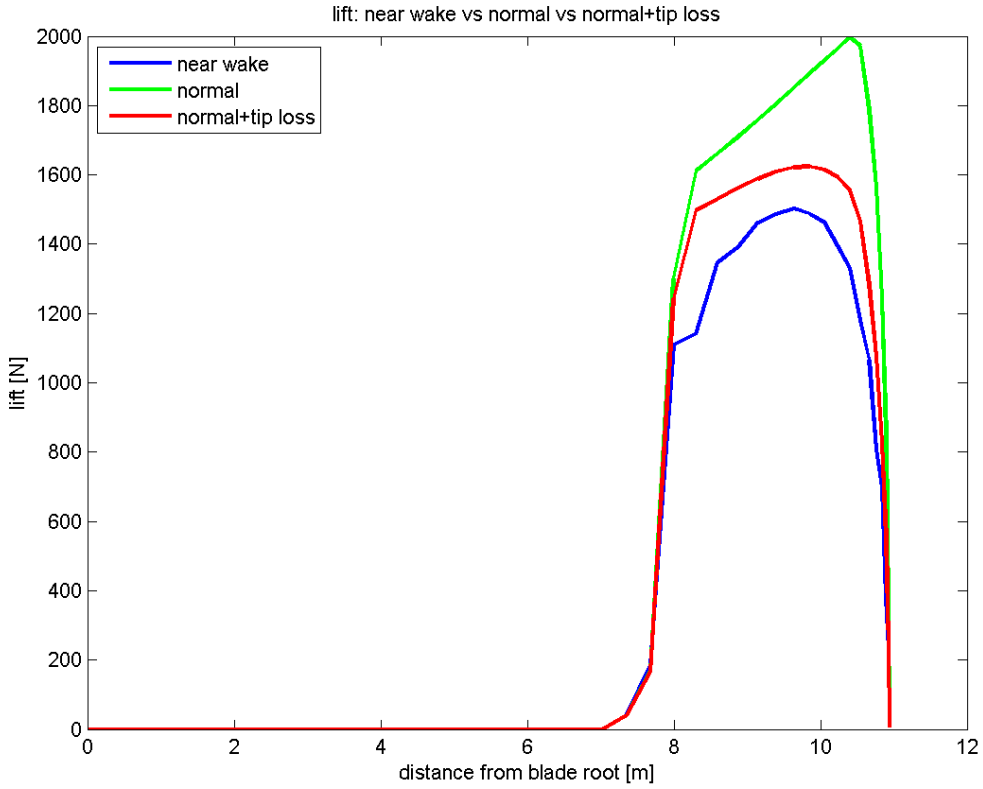

Figure 81 - Comparison of computed lift per element along boom span (V=10m/s, ω=50rpm, pitch=0deg.).

Modal analysis

In order to identify the system dynamics, modal analysis is performed on the aeroelastic model of the rotating rig in HAWC2. The full turbine modes are captured for different configurations and the lowest ones are presented in **Table 16**.

Table 16 - Predicted full turbine modes.

Case	Mode 1		Mode 2		Mode 3		Mode 4		Mode 5	
	f [Hz]	δ [%]	f [Hz]	δ [%]	f [Hz]	δ [%]	f [Hz]	δ [%]	f [Hz]	δ [%]
Stiff tower – fixed shaft	-	-	-	-	1.2	10	1.5	7	3.7	24
Stiff tower – free shaft	-	-	-	-	-	-	1.5	7	2.9	0.7
Flexible tower - fixed shaft	0.8	0.2	1.1/1.1	0.3/0.8	1.2	9	1.5	7	4	24

Flexible tower - free shaft	0.8	0.1	1.1/1,1	0.3/0.4	-	-	1.5	7	3.2	2.5

With the stiff tower configuration and a fixed shaft degree of freedom, the lowest predicted modal frequencies correspond to full rotor in-plane (1.2Hz), out-of-plane (1.5Hz), and in-plane asymmetric (3.7Hz) rotor modes. With the stiff tower configuration and free rotation shaft degree of freedom, the lowest predicted modal frequencies correspond to out-of-plane (1.5Hz) and in-plane asymmetric (2.9Hz) rotor modes. Adding the tower flexibility generates three tower modes, (0.8Hz, 1.1Hz, and 1.1HZ), corresponding to torsion, fore-aft, and side-to-side vibration directions, respectively.

Controls

In the aeroelastic simulations described in this section, which are relevant for the design of the rotating rig, the rotor speed, pitch and flap angles are all prescribed with input command signals utilizing a type2 DLL. A standard 2nd order pitch servo model is implemented to simulate the pitch dynamics, assuming a pitch system with natural frequency 0.4Hz and damping ratio 0.7.

Prediction of aeroelastic loads

Aeroelastic loads are predicted utilizing the described model for a range of load cases, focusing on extreme loading during normal operation cases. Loads are calculated at 120s simulations for 4 load cases, for which the main operating parameters are shown in **Table 17**.

Table 17 – Loads cases for aeroelastic loads in the HAWC2 model.

load case	type	wind speed	turbulence intensity	wind shear	rpm	pitch
1	normal	10	0.1	log 0.2	50	0
2	wind ramp	5 to 15	0.1	log 0.2	50	0
4	rpm ramp	10	0.1	log 0.2	10 to 60	0
3	pitch sine	10	0.1	log 0.2	50	Harmonic, 2.5deg, 1Hz

The time varying load response on the boom is shown by plotting the flapwise root bending moment and the aerodynamic characteristics (angle of attack and lift coefficient) in the middle of the wing section along with the freestream hub height wind speed.

Load case 1 (**Figure 82**) is considered representative of the extreme range of normal operation during the experimental campaign, where the rotor speed is fixed at a maximum of 50rpm and reference wind conditions are simulated. The aerodynamic characteristics of the aerofoil section in this case are close to a full scale operation.

Load case 2 (**Figure 83**) is simulating an increase of wind speed from 5m/s to 15m/s, checking for the effect on the aeroelastic response. The maximum (negative) flapwise moment is seen increase up to 50% compared to load case 1.

Load case 3 (**Figure 84**) is used to check the load response for a range of rotational speeds ranging from 10rpm to 60rpm. It is seen that load variations are increased up to 50% for rotational speeds above 40rpm compared to ones at 30rpm.

Load case 4 (**Figure 85**) simulates a harmonic excitation of the pitch at a maximum range of operation with a demand angle to the pitch servo of +/-2.5deg at 1Hz, which results in considerable increase in the flapwise blade root moment and it is also relevant for the loading on the pitch system. The torsional moment at the pitch bearing is shown in **Figure 86**. The

maximum moment is found to be 1.6 kNm. It is found, though that load case 2 introduces a higher pitch bearing moment of 1.8 kNm while wind speed rises to 16m/s, as shown in **Figure 87**.

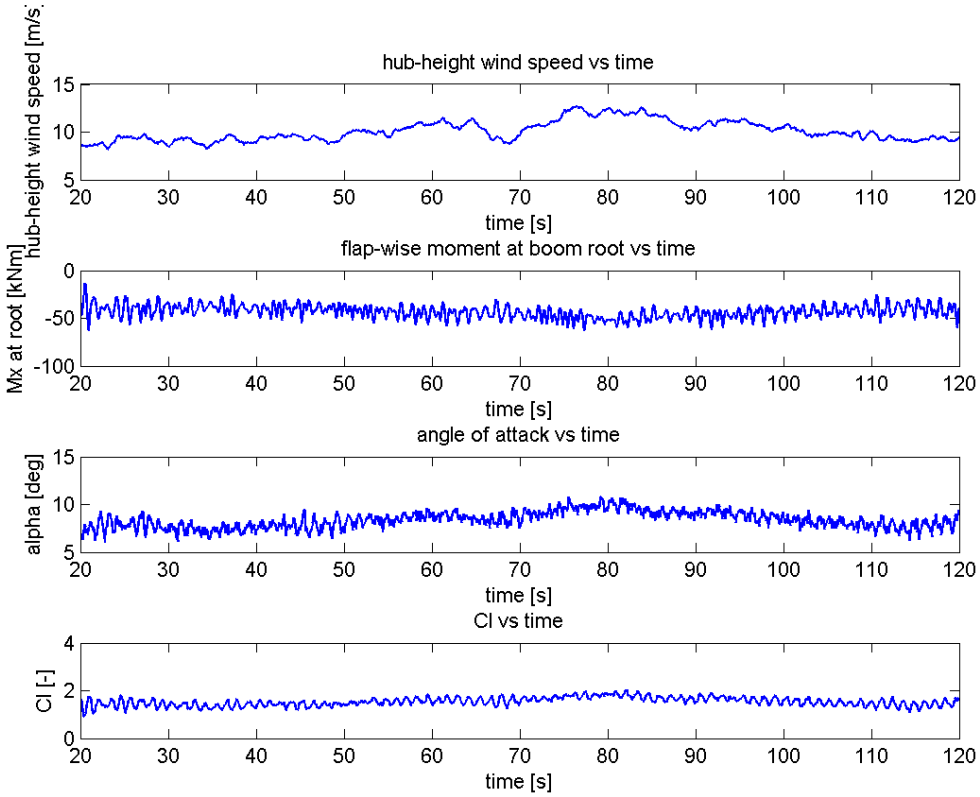

Figure 82 - Results load case 1: Normal.

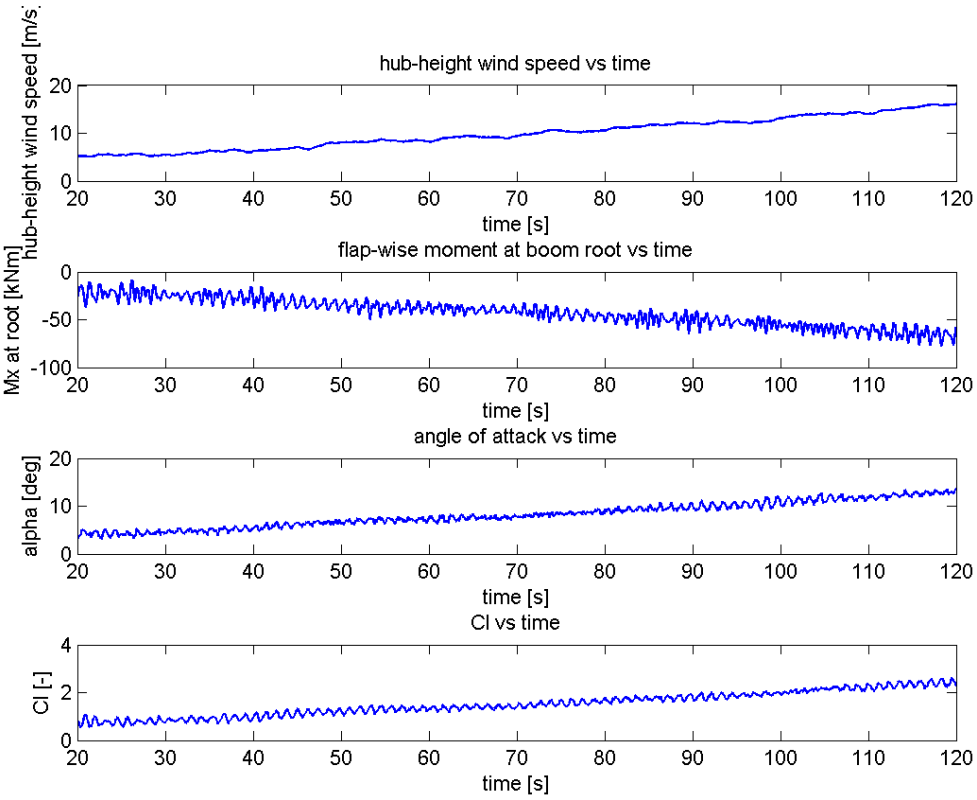

Figure 83 - Results load case 2: Wind ramp.

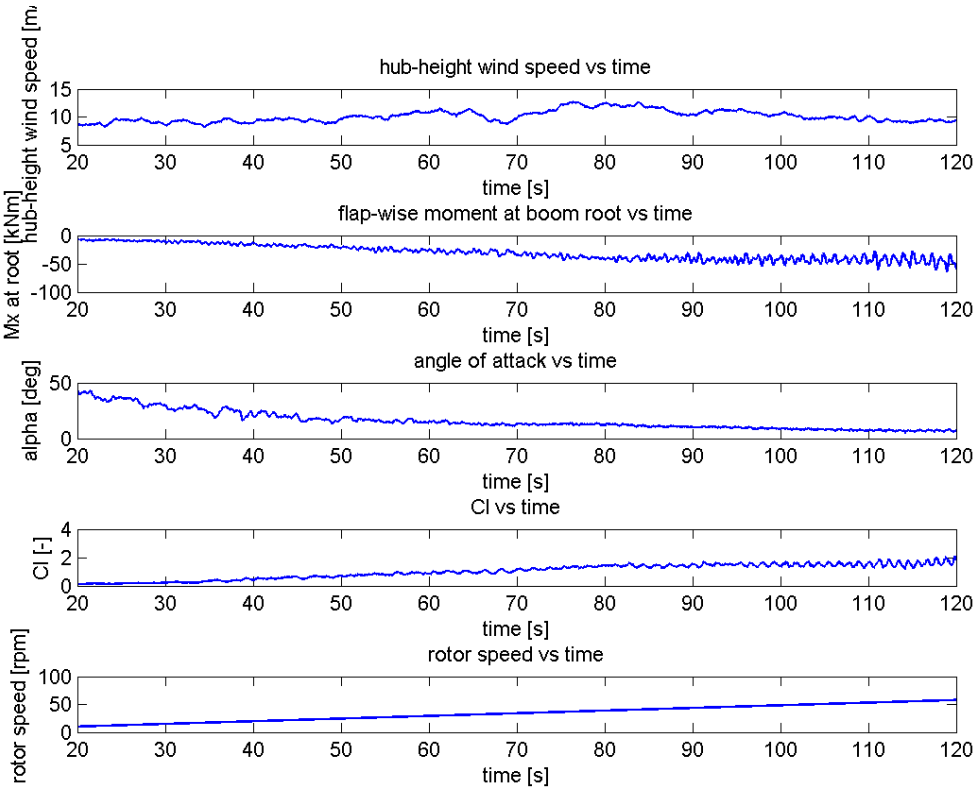

Figure 84 - Results load case 3: rpm ramp.

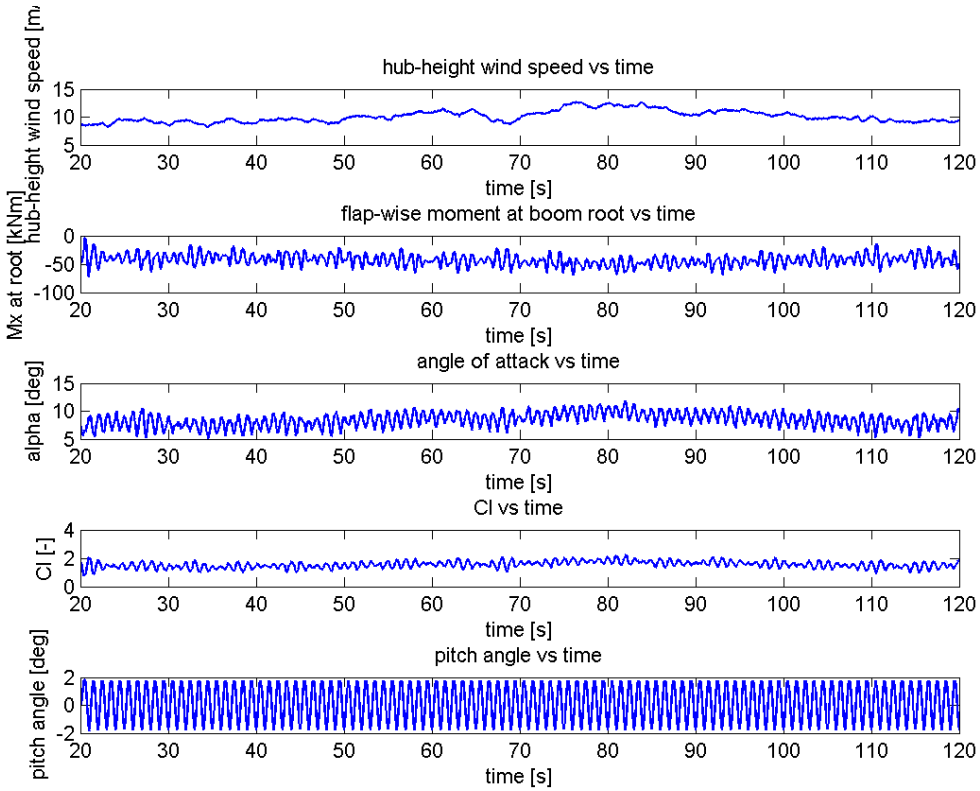

Figure 85 - Results load case 4: Pitch sine.

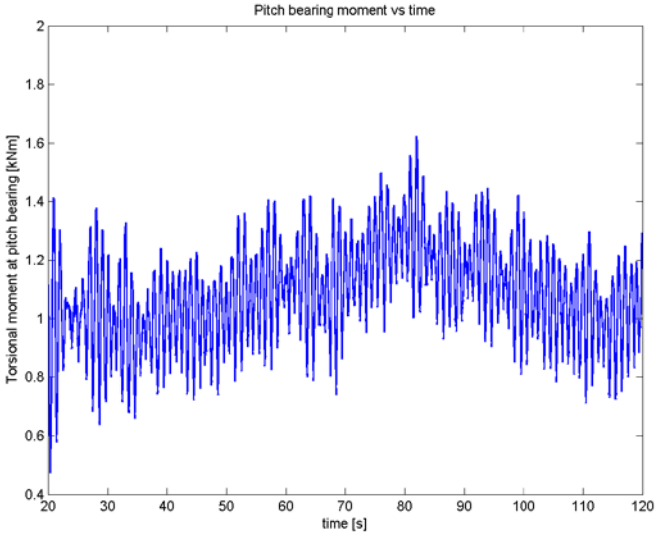

Figure 86 – Case 4: Time response of the torsional moment at the pitch bearing.

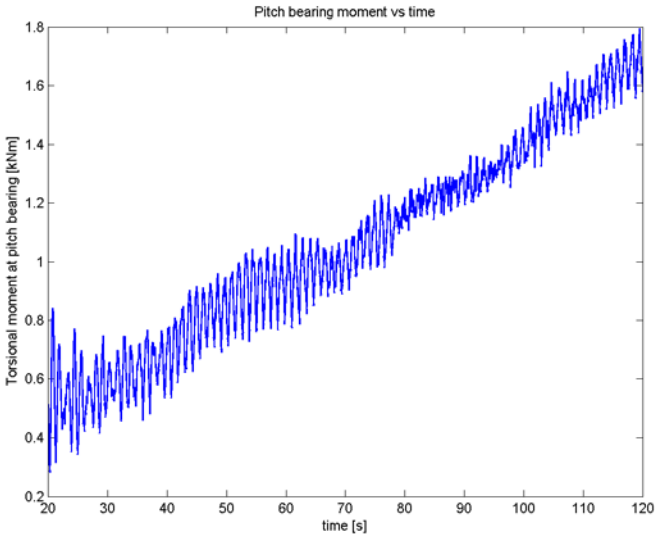

Figure 87 – Case 2: Time response of the torsional moment at the pitch bearing.

Furthermore, for every load case, the distributed average and maximum stress level along the boom span are calculated, in order to validate the boom design with the latest HAWC2 model. A range of representative sections are chosen at the origin of every component (as described in **Section 2**), and the geometrical parameters of the thin walled cylindrical section are used together with the resulting sectional bending moment ($M_{x)}$ and normal force (F_z, in the spanwise direction) from HAWC2. The resulting maximum stress is calculated according to **Eq. 18**, where the sectional area and area moment of inertia is calculated according to the inner and outer diameter of the cylindrical sections, and the outer diameter is used as the maximum distance from the centre.

$$\sigma_{max} = \frac{N}{A} + \frac{M \cdot y_{max}}{I} \qquad \textbf{(Eq. 18)}$$

The resulting average and maximum flapwise moment, normal force and stress distributions for load cases 1, 2, 3, and 4 is shown in **Figure 88**, **Figure 89**, **Figure 90**, **Figure 91**, respectively.
It is seen that maximum stresses occur close to the root and close to the wing section connection. Load case 2 with the increase of wind speed up to 15 m/s introduces the highest value of 114 N/mm^2 close to the root. This is much lower compared to the computed stress levels used for the boom design as seen in **Figure 5**, as well as the 0.2% proof stress of the materials**.**

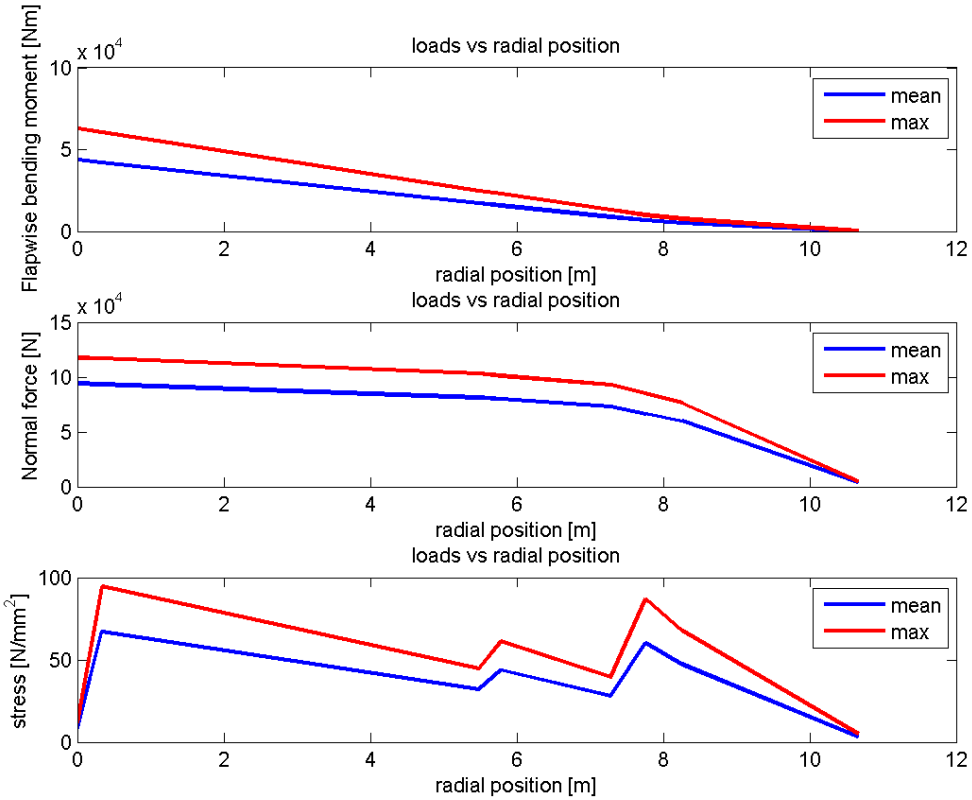

Figure 88 – Distributed load and stress load case 1: Normal.

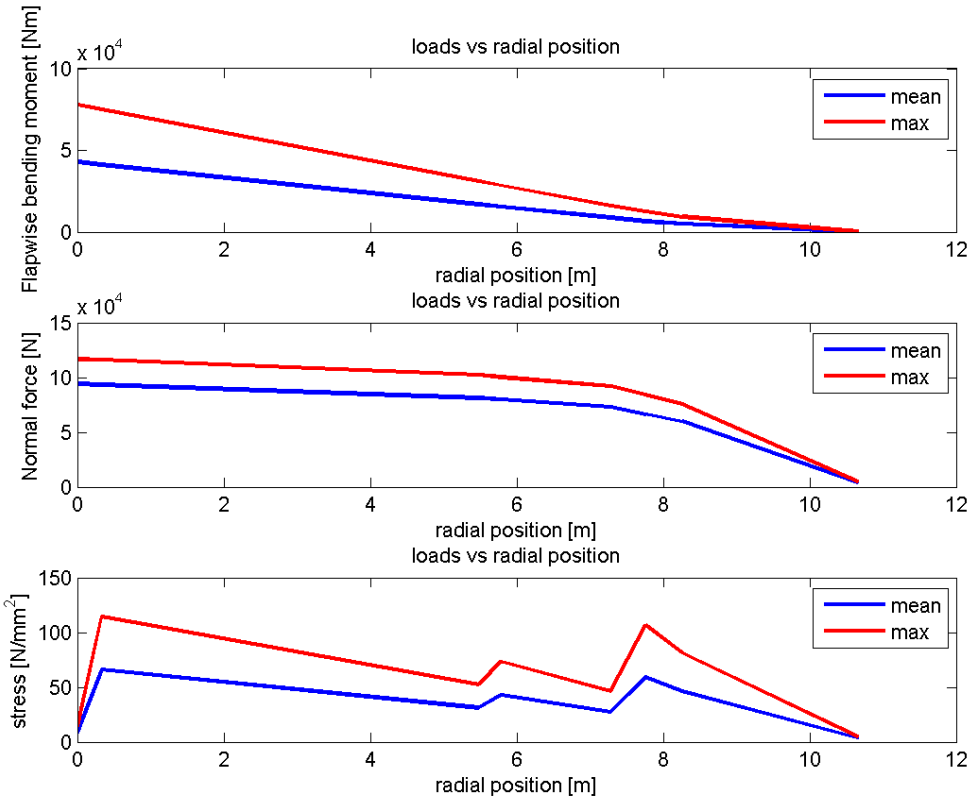

Figure 89– Distributed load and stress load case 2: Wind ramp.

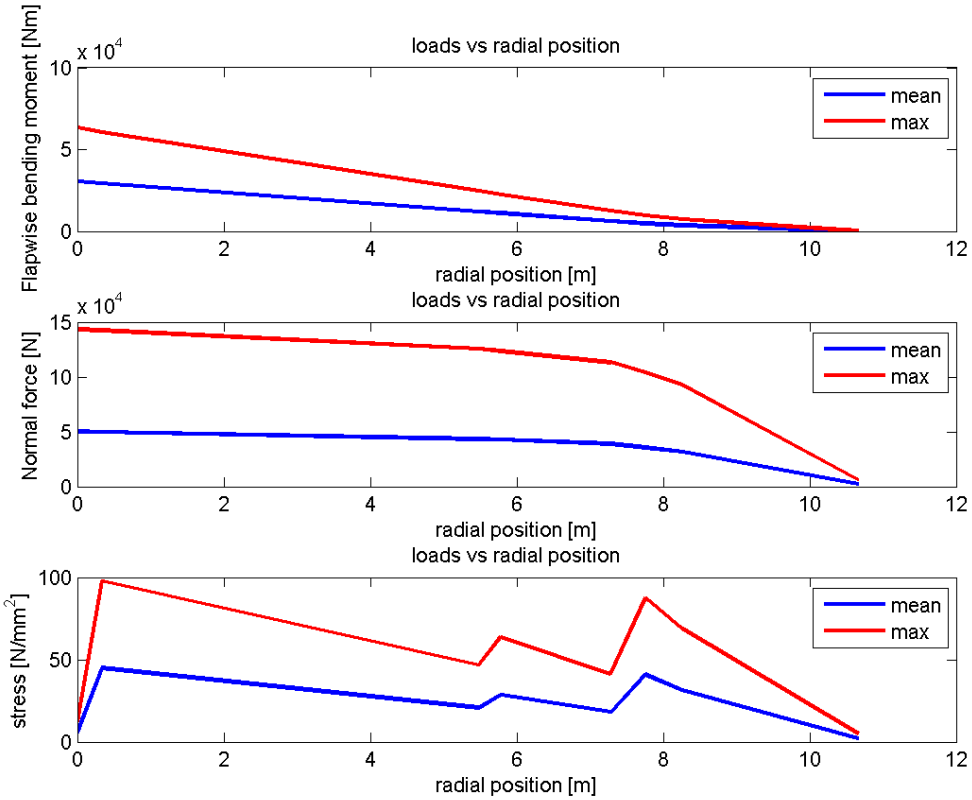

Figure 90– Distributed load and stress load case 3: Rpm ramp.

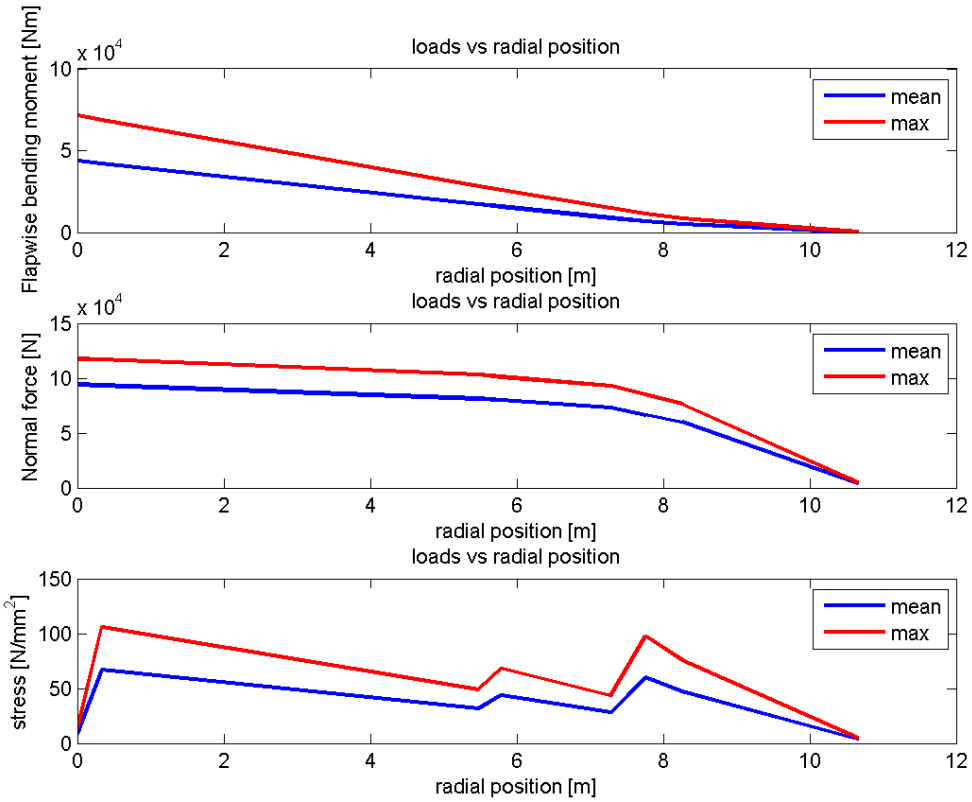

Figure 91– Distributed load and stress load case 4: Pitch sine.

8. Experimental data on the test rig dynamics

This section describes two methods of estimating the dynamics of the rotating rig in a standstill configuration.

Modal analysis using a hammer excitation test

The B&K PULSE system is used on 25-07-2014 in order to perform a modal analysis test on the rotating rig. Two charge accelerometers are placed close to the aerofoil section connection point with the boom (approx. 7.2m from the blade root), and an impact hammer with a force transducer is utilized for the system excitation. The accelerometers are measuring in the flapwise and edgewise directions. The boom is free to rotate by releasing the rope locking it to the tower.

Two tests with hammer impact are performed and one with no hammer impact and excitation by means of manually pulling the boom. Post-processing of the captured data is performed by calculating the amplitude of the complex frequency response function and plotting it for the first two cases (**Figure 92**, **Figure 93**), and then plotting the auto spectrum and time series of the sensor response in the third case (**Figure 94**, **Figure 95**).

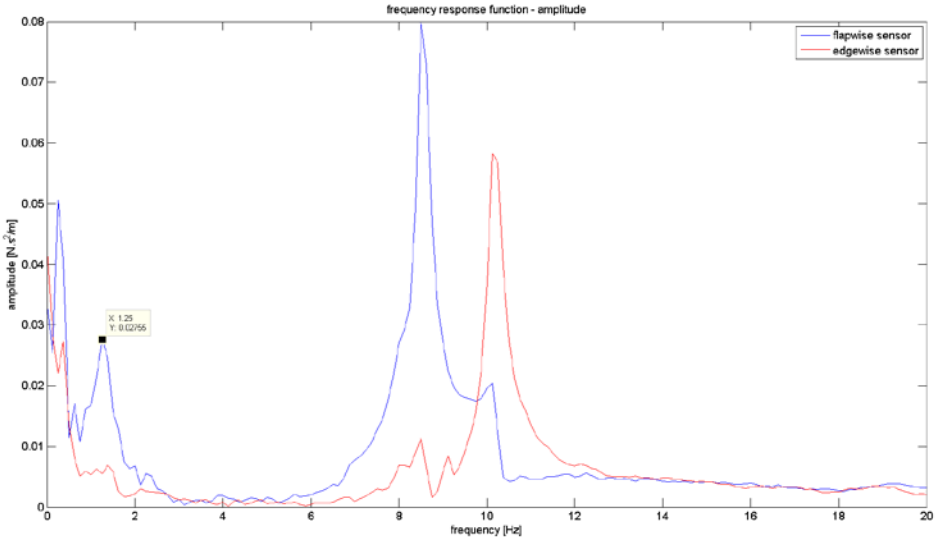

Figure 92 – Frequency response of hammer impact test 1.

Based on the first test, the flapwise sensor captures three dominant peaks at 0.25Hz, 1.25Hz and 8.5Hz. The peak at 1.25Hz is most probably the one corresponding to the first flap-wise vibration mode. The edgewise sensor captures one peak at 10.13Hz.

Using the 'half power bandwidth method' the damping ratio of the 1.25Hz mode can be estimated:

$$\zeta = \frac{\omega_2 - \omega_1}{2 * \omega_n} \cong \frac{1.45 - 1.04}{2 * 1.25} \cong 0.164 \quad \textbf{(Eq. 19)}$$

, where ω_1 and ω_2 are the frequency limits on the peak corresponding to the half-power (-3db) amplitude level:

$$\frac{Amp_{max}}{\sqrt{2}} \cong \frac{0.02755}{\sqrt{2}} \cong 0.0195 \quad \textbf{(Eq. 20)}$$

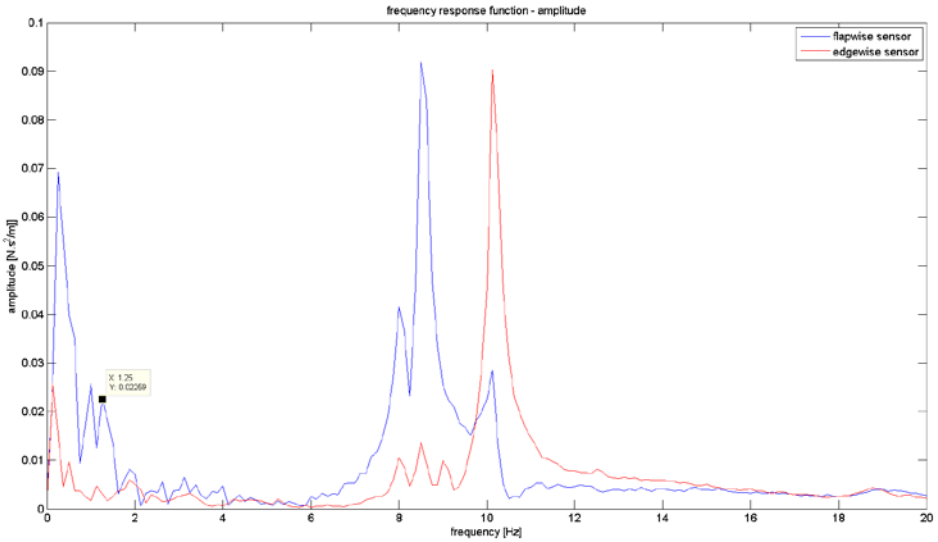

Figure 93 - Frequency response of hammer impact test 2.

Based on the second test, the flapwise sensor captures three dominant peaks at 0.25Hz, 1Hz-1.25Hz and 8.5Hz. The peak at 1.25Hz is most probably the one corresponding to the first flap-wise vibration mode. The edgewise sensor captures one peak at 10.13Hz.

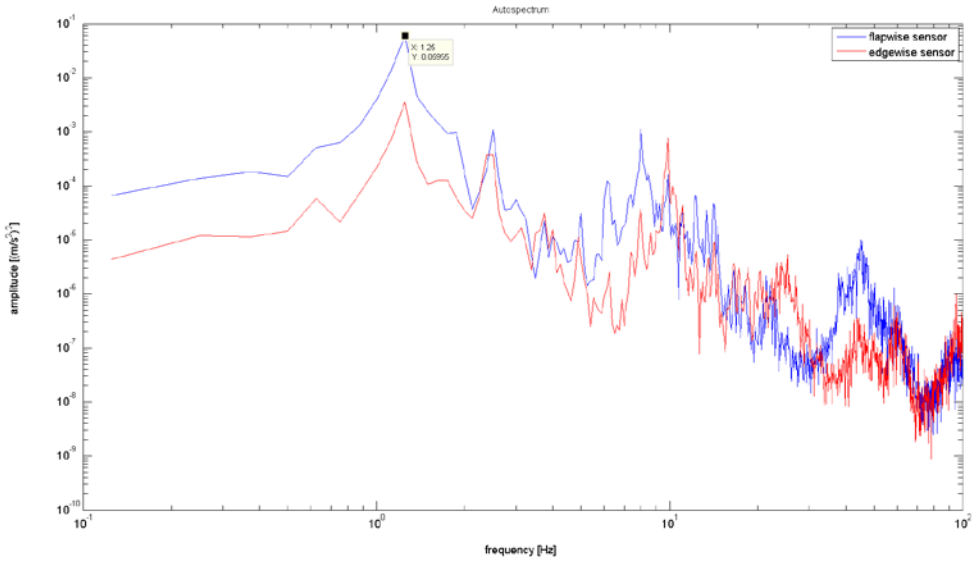

Figure 94 – Auto-spectrum of pull excitation test.

Based on the pull excitation test, the dominant free vibration mode visible in both sensors is estimated at 1.25Hz, most probably the one corresponding to the first flap-wise vibration mode. A peak at 2.5Hz is also captured from both sensors.

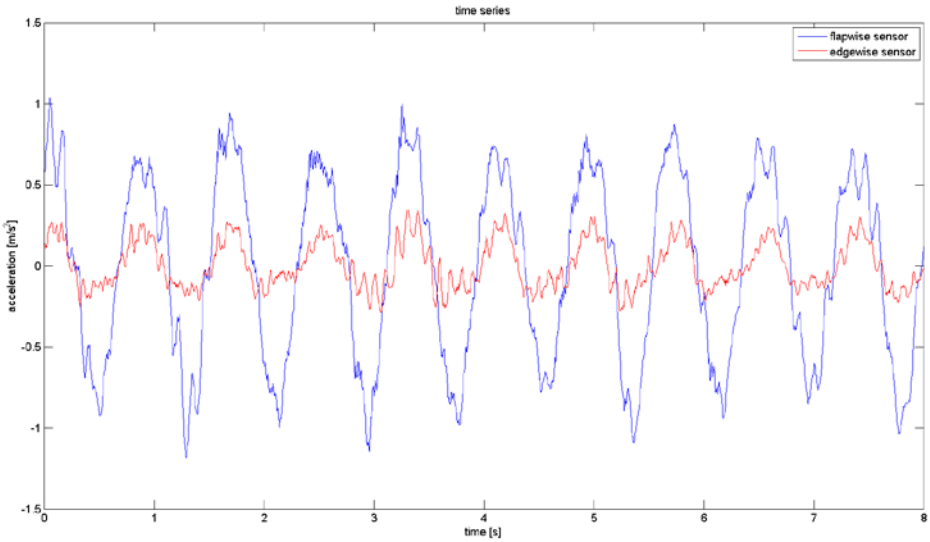

Figure 95 – Time series of strain signal during pull excitation test.

In the time series of the signals the dominant free vibration mode (1.25Hz) is visible from both sensors. The higher frequency content (8.5Hz-10.13Hz) is also visible.

System identification using strain signal data in normal wind excitation

Strain gauge data from measurements on the rotating rig during standstill conditions on 21-08-2014 are processed in order to estimate the modal characteristics of the boom. 10-min data sets from 08:30 to 10:30 are processed (130min in total). The spectra of the captured data for the flapwise and edgewise sensors are shown in **Figure 96**.

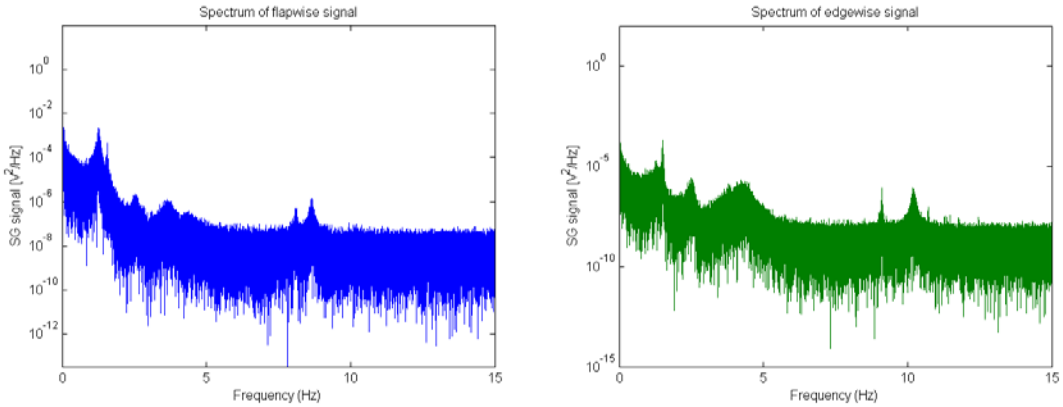

Figure 96 – Spectra of captured signals.

The N4SID subspace system identification method is used and 16th order linear state-space models are identified for the data from the flapwise or the edgewise strain sensor, with reasonable accuracy. The comparison of measured and simulated time response of the two sensors is shown in **Figure 97**.

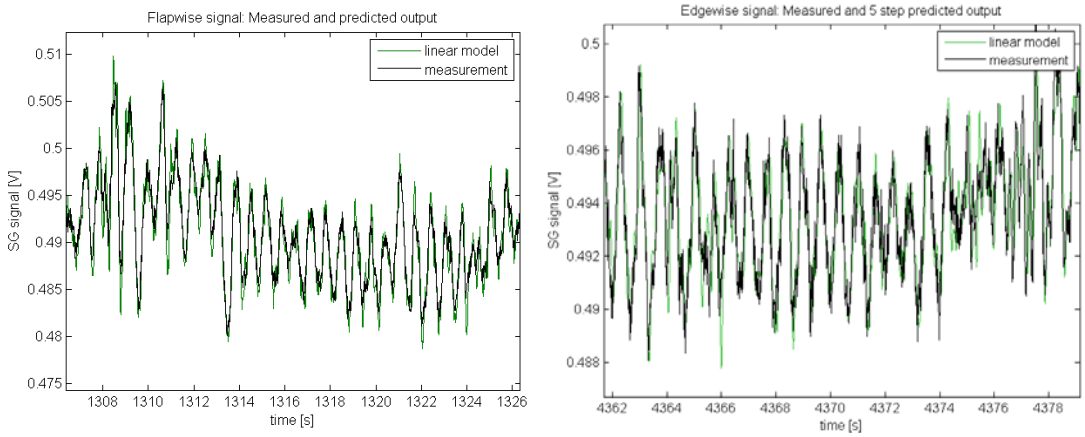

Figure 97 – Time series comparison: measurement and linear model predictions.

Natural frequency and logarithmic damping are extracted from the linear model for the two lowest modes and are presented in **Table 18**.

Table 18 - Identified modal characteristics

case	time	order	fit [%]	f_1 [Hz]	f_2 [Hz]	δ_1 [%]	δ_2 [%]
flap	08:30-10:30	16	93	1.29	2.54	19	-
edge	08:30-10:30	16	82	1.45	4.39	32	41

The identified first flapwise mode corresponds reasonably with the hammer test results and the aeroelastic model predictions. The identified second flapwise mode also corresponds to the pull excitation tests results. The identified edgewise models are only comparable with the numerical predictions. Generally all tested methods have shown a variation in the prediction of modal frequencies, but provided the more insight into the modal characteristics of the setup. Further analysis is required for more detailed predictions and use of results for model tuning.

References

[1] Bak, C. et al., DANAERO MW: Instrumentation of the NM80 turbine and meteorology mast at Tjæreborg, DTU Wind Energy Report-I-0083, 2013.

[2] Larsen, T. B., Hansen A. M., (2013): How 2 HAWC2, the user's manual, Risø-R-1597(ver. 4-4) (EN).

[3] Madsen, H. A., (1991): Structural Dynamics of a 100kW HAWT, Risø-M-2887.

[4] Bergami, L., Gaunaa, M., (2012): ATEFlap Aerodynamic Model, a dynamic stall model including the effects of trailing edge flap deflection, Risø-R-1792(EN).

[5] Pirrung, G. R., Hansen, M.H., Madsen, H. A., (2012): Improvement of a near wake model for trailing vorticity, Conference on the Science of Making Torque from Wind, Oldenburg, Germany, 2012.

Acknowledgements

The work of the following colleagues who have contributed to the design of the rotating rig is acknowledged:
Peter B. Andersen, Leonardo Bergami, Jacob Christensen, Christian Madsen, Jonas Heininge, Malte Markussen, Karen Enevoldsen, Per Hansen , Kasper Clemmensen, Michael Rasmussen, Lars Christensen, Oluf Høst, Erik Juul, Johnny E. Jørgensen, Michael Nimb, Jan S. Andersen.

DTU Wind Energy is a department of the Technical University of Denmark with a unique integration of research, education, innovation and public/private sector consulting in the field of wind energy. Our activities develop new opportunities and technology for the global and Danish exploitation of wind energy. Research focuses on key technical-scientific fields, which are central for the development, innovation and use of wind energy and provides the basis for advanced education at the education.

We have more than 240 staff members of which approximately 60 are PhD students. Research is conducted within nine research programmes organized into three main topics: Wind energy systems, Wind turbine technology and Basics for wind energy.

Danmarks Tekniske Universitet
DTU Vindenergi
Nils Koppels Allé
Bygning 403
2800 Kgs. Lyngby
Phone 45 25 25 25

info@vindenergi.dtu.dk
www.vindenergi.dtu.dk